# Integrated study of water Sr isotopes and carbonate Sr-C-O isotopes reveals long-lived fluid compartments in the Langfjellet Oil Discovery, Norwegian North Sea

Farhana Huq[1*], P. Craig Smalley[2], Viktoriya Yarushina[1], Ingar Johansen[1], Christian Alexander Schöpke[1], Lena K. Øvrebø[4], Elin Skurtveit[3], and Ebbe H. Hartz[4]

[1] Institute for Energy Technology, Instituttveien 18, NO-2007 Kjeller, Norway

[2] Department of Earth Science & Engineering, Imperial College, London SW7 2AZ, UK

[3] Norwegian Geotechnical Institute, Sognsveien 72, 0806 Oslo, Norway

[4] Aker BP ASA, Oksenøyveien 10, 1366, Lysaker, Norway

*Corresponding author: Farhana Huq

e-mail: farhana.huq@ife.no

## Abstract

Routine measurements of reservoir pressure variation with depth can detect pressure discontinuities indicative of barriers to vertical fluid movement. This study investigates how pressure data can be augmented by detailed profiles of formation water $^{87}Sr/^{86}Sr$ ratio to determine the precise location and cause of such barriers, and by C-O-Sr isotope analysis of carbonate cements to determine the duration over which the barrier has persisted. The study focuses on the clastic Hugin Formation reservoir in the Langfjellet Oil Discovery (Norwegian North Sea). Here, pressure data indicated a barrier somewhere within a 25 m depth interval. Formation water $^{87}Sr/^{86}Sr$ was measured with high spatial resolution by extraction from core samples using the residual salt analysis (RSA) method. This revealed three homogeneous populations of water separated by a small step in $^{87}Sr/^{86}Sr$ over a 7 m interval containing coal and shale layers, and a very large step in $^{87}Sr/^{86}Sr$ over a 1.2 m interval corresponding to a thin coal and shale layer situated below a major flooding surface. The latter is the main candidate for the pressure barrier. Modelling confirmed that this inferred pressure barrier also greatly retards Sr diffusion.

Carbonate cements occur disseminated throughout the reservoir and in several heavily-cemented zones. Oxygen isotope-derived temperatures indicate that these formed in two episodes: (1) Pre-compactional, precipitated shortly after deposition in the zone of bacterial methanogenesis (~30ºC, ~200 m depth, ~162 Ma); (2) Post-compactional incorporating thermal decarboxylation-derived carbon (~90ºC, ~2500 m depth, ~46 Ma). Carbonate $^{87}Sr/^{86}Sr$ data reveal the same compositional populations present in the

current formation water to be present in both cement generations. The water compositional stratification must thus have been present when the early and late cements precipitated, down till today. The persistence of a compositional step for most of the geological history of the rocks confirms the presence of a major fluid communication barrier. The Sr RSA data show invariant water composition across the heavily carbonate cemented intervals, implying no barrier effect.

The combination of pressure data (to identify pressure barriers), Sr RSA (to add spatial resolution) and Sr-C-O isotopes of carbonates of different ages (to add a time dimension) is useful for identifying major long-term fluid communication barriers and differentiating them from smaller, less effective or shorter-term features. The method has applications for identifying seals in exploitation of petroleum and water resources, and underground storage of $CO_2$ and radioactive waste.

**Keywords:** Carbonate cement, fluid communication, Sr isotopes, C isotopes, O isotopes, barrier, compartments

# 1. Introduction

In many situations where the subsurface is exploited by extracting fluids (e.g., oil and gas production, potable water resources), injecting fluids (e.g., water or hydrocarbon gas for oil production or $CO_2$ for enhanced oil recovery or permanent storage), cycling fluids (e.g., geothermal resources), or safely storing undesired substances (e.g., $CO_2$ or radioactive waste), it is critical to understand barriers to vertical fluid flow in order to determine project feasibility and optimize project design. For example, large-scale flow barriers in sedimentary systems affect leakage risk in $CO_2$ (Huq et al., 2017) or radioactive waste storage projects, and petroleum trapping potential for petroleum exploration (Brommundt et al., 2014; Elenius et al., 2018; Løseth et al., 2009). Such barriers need to be effective over many thousands or millions of years. Identifying barriers to vertical fluid movement within reservoirs is important during appraisal of new oil or gas discoveries, because fluid communication in the reservoir, or the lack of it, can have a large impact on reservoir performance factors such as drainage and sweep efficiencies, thus affecting the rate and amount of oil or gas recovery and project economics (Jolley et al., 2010; Fokker et al., 2012; Smalley et al., 1994; Smalley & Muggeridge, 2009). If barriers to fluid communication are identified during appraisal, these can be taken into account when making key development decisions, such as choice of recovery process, number, type and position of wells, well completion intervals – as well as whether or not to develop a field at all.

Similarly, the presence of smaller scale baffles (i.e., barriers that have limited size or effectiveness) can control the dispersion of injected $CO_2$ in subsurface storage projects (chapter 10 in Woods, 2015; Cavanagh and Haszeldine, 2014); if such baffles are

identified, they can be exploited by positioning injectors to direct $CO_2$ towards the desired storage locations. In water resources management, fluid flow barriers or baffles can help protect aquifers from overlying contaminants, for example from landfill sites (Labus et al., 2020).

Barriers or baffles to vertical fluid flow can be caused by a variety of geological features. Examples include: stylolites (Toussaint et al., 2018), faults and deformation bands (Antonelli et al., 1999; Choi et al., 2015; Griffiths et al., 2016; Japsen et al., 2011), diagenetic zones such as carbonate-cemented layers (Cui et al., 2017; Dutton et al., 2002; Fayek et al., 2001) and laterally extensive shales (Smalley & Hale, 1996; Fox & Bowman, 2010; Elenius et al., 2018).

Potential barriers and baffles can be identified by descriptive work, such as geological mapping, well logging, core analyses, high-resolution stratigraphy etc. (Doughty et al., 2008; Jackson et al., 2019). However, such data are static, and do not directly measure the barrier effect of the described features. In appraisal of oil and gas fields and potential $CO_2$ sites, hydraulic well testing routinely provides dynamic information based on pressure transmission on a timescale of hours to days (Doughty et al., 2008). Pressure monitoring during oil or gas production may provide dynamic information on a timescale of years. For a longer timescale, relevant for $CO_2$ storage, nuclear waste disposal or oil exploration, natural pressure distributions can be used, along with reservoir geochemistry. Variations in natural pressure and reservoir geochemistry (including fluid composition and density) contain dynamic information on a geological timescale; such variations have a propensity to mix through time due to pressure-driven flow, density-driven advection or diffusion, processes that can be modelled. Where

sufficient time has elapsed for such differences to have equilibrated, yet they have not, this indicates the presence of a barrier, and the degree of excess disequilibrium is a measure of barrier strength and/or lateral extent (Smalley & Muggeridge, 2010; Smalley et al., 2020).

Natural pressure variations are often viewed as definitive for identifying flow barriers, but such data suffer from two limitations. Firstly, measurements, particularly in offshore situations, are expensive, and the number of pressure measurements are thus limited and the measurement points widely spaced, so that even if the presence of a barrier is detected its exact position and the geological feature causing it, may remain uncertain. Secondly, pressure equilibrates relatively rapidly (compared, say, to fluid composition; Smalley & Muggeridge, 2010), so pressure may give only limited information about the longevity of barrier behaviour on a geological timescale. Although the presence of a step change in pressure across, say, a shale layer may confidently be interpreted to indicate a flow barrier, lack of a pressure step could mean either: (a) there is no barrier; (b) there is a barrier, but no pressure difference ever evolved across it; or (c) there is a barrier and there once was a pressure step, but it has now dissipated. To distinguish between these alternatives, other data are required.

In this study we employ a combination of two techniques in addition to pressure variations to address vertical fluid communication over geological time:

- Detailed profiles of current formation water $^{87}Sr/^{86}Sr$ variation with depth, sampled using the residual salt analysis (RSA) method from core (Smalley et al. 1995; Mearns and McBride, 1999). This provides information at the timescale of diffusional mixing of Sr in water (Smalley et al., 2020), a longer timescale than

pressure equilibration. We demonstrate how the greater vertical resolution of the Sr RSA data compared to pressure helps define the exact position, nature and effect of potential barriers to fluid communication.

- Analysis of $^{87}Sr/^{86}Sr$ in carbonate cements, which reflects the water composition at the time various cements of different ages were precipitated, along with stable C and O isotopes to determine the source of carbon and, importantly, the temperature and timing of cementation (Liang et al., 2019; Li et al., 2011; Walderhaug and Bjørkum, 1992; Cai et al., 2010; Basin et al., 2009). This allows water $^{87}Sr/^{86}Sr$ compositional variations to be reconstructed, and barrier effectiveness to be evaluated, over much of the geological history of the rocks.

The study demonstrates how isotopic analyses of water and carbonate cements combined with analytical modelling can help to identify and quantify flow barriers through time. The results are used to evaluate geological features such as shale, coal and carbonate-cemented layers, to determine whether or not they form flow barriers and, if so, their likely effectiveness and duration. Where the presence of a barrier is indicated by pressure data, the results demonstrate how additional isotopic data can pinpoint barrier location and thus its likely cause.

# 2. Background

## 2.1 Geological setting

The study site is the Langfjellet Oil Discovery, located on the Norwegian Continental Shelf in the central North Sea, 20 km east of the Frigg field, on the eastern flank of the Viking Graben (Figure 1). This is a deep Jurassic to Cretaceous basin in which thermally mature Late Jurassic organic shales provide the source for many nearby oil and gas fields. Overall, the Mesozoic geology records both continued basin formation, and deepening waters in the area. The studied reservoir interval is in the Mid Jurassic Hugin Formation, at about 3500 m depth. In the Mid Jurassic, the sea transgressed from the Northwest into the Langfjellet area. In this region, the fluvial to lower coastal plain deposits of the middle Jurassic Sleipner Formation first interfinger with, and then are gradually overlain by, the shallow marine Hugin Formation. In the study area, there is a sharp transition from the Sleipner Formation into the overlying Hugin Formation, reflecting the transition from lower coastal plain to shoreface deposition (Figure 2). The sandstones of the upper Hugin Formation are in turn draped by the marine shales of the Late Jurassic Heather and Draupne formations.

The Hugin Formation consists of fairly well-sorted fine to coarse grained sandstones, interlayered with shales and siltstones (Kieft et al., 2011; Folkestad and Satur, 2008). In Langfjellet, the Hugin Formation is subdivided by the field operator into 5 reservoir units (H1-5; Figure 2) reflecting deposition with a variable sea level ranging from marginal marine to lower shore face. The succession of mainly sandy prograding parasequences of H1, and the sandy H2 zone, are overlain by an interval of organic-rich shales and coal beds (H3), deposited within a paralic setting of interdistributary bays. At the top of

H3 is a transgressive surface and the overlying H4 interval is shaley sand topped by a thin coal and shale layer and an overlying flooding surface. This passes upwards into the sandy H5 interval.

The study focuses on well 25/2-18 S (Figure 1), which terminated in the Sleipner Fm, and its twin 25/2-18 ST2 that was drilled as a technical sidetrack for coring purposes, terminating in the Hugin Fm.

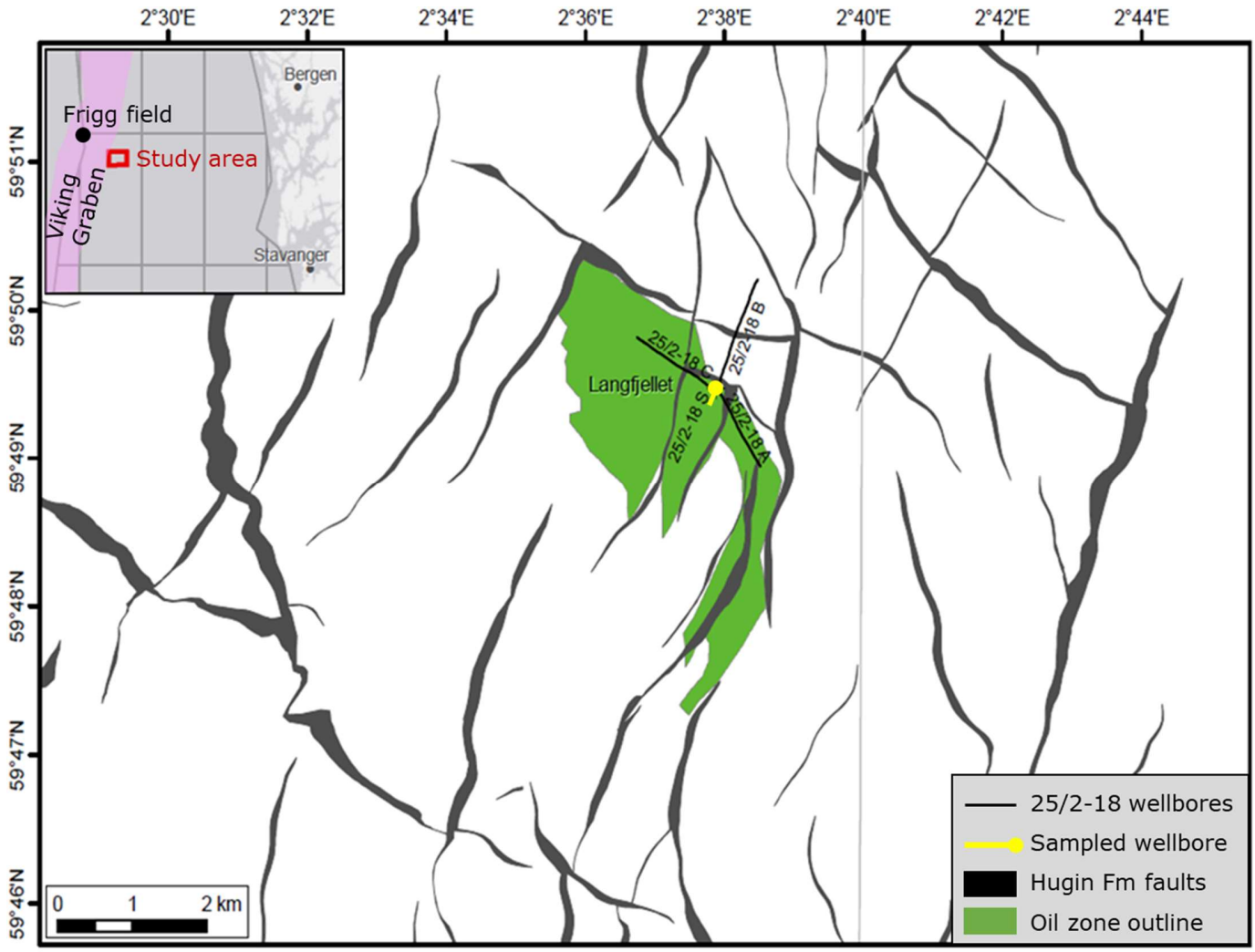


**Figure 1. Location (inset) and configuration of the Langfjellet Oil Discovery relative to faults at the top Hugin level. Green denotes outline of oil presence. The 25/2-18S well is shown in yellow. The sampled well 25/2-18ST2 is a technical sidetrack to this well for coring purposes, which follows a similar trajectory.**

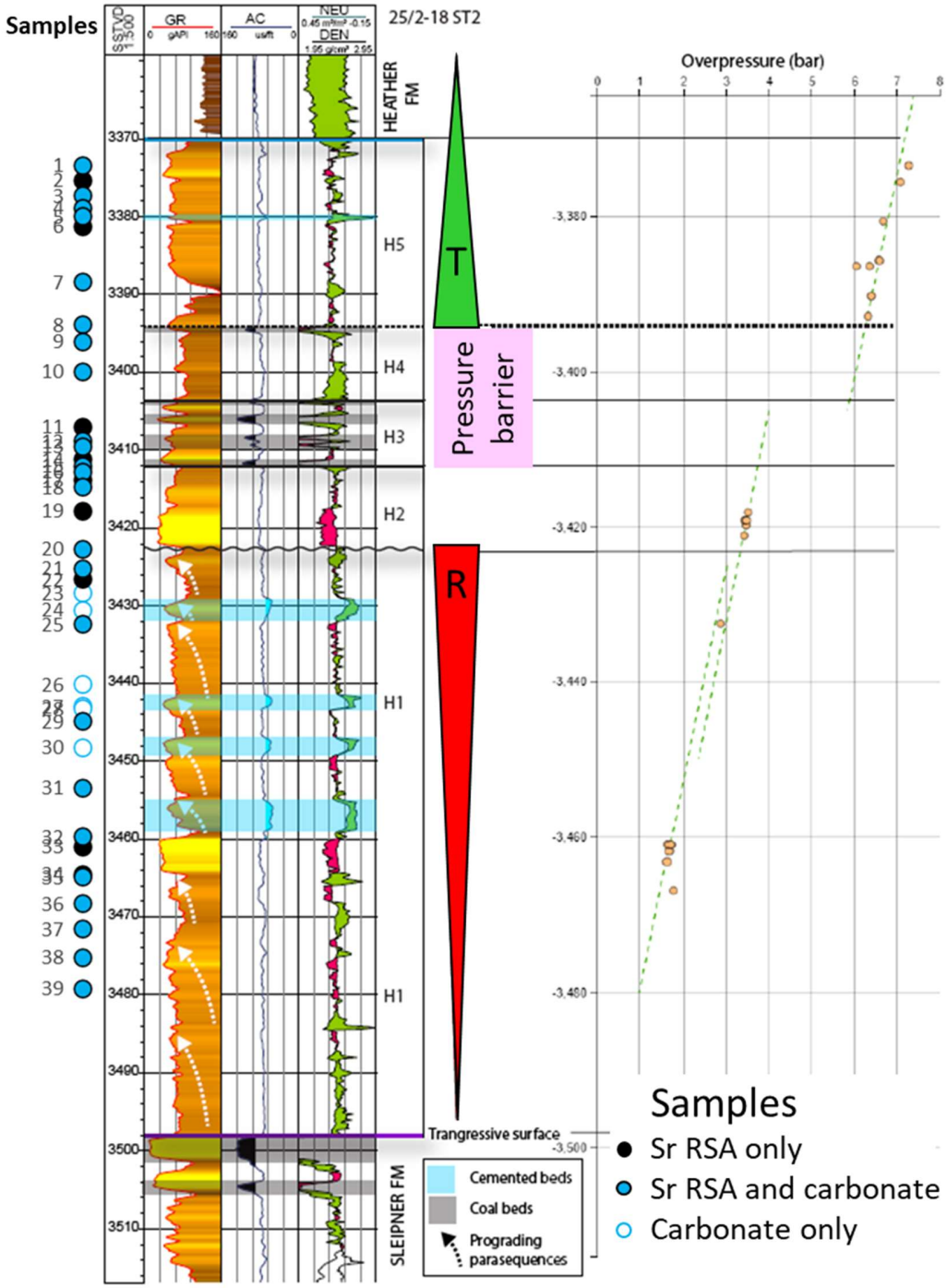


**Figure 2. Stratigraphy of the Hugin Formation in well 25/2-18 ST2. Gamma ray (GR), acoustic (AC), neutron (NEU) and density (DEN) logs are shown, along with lithology and Hugin zonation (H1-H5). R = sea level regression, T = sea level transgression. Coals are identified by the negative (black-shaded) deviations in AC, shale content by high gamma values and green-shaded crossovers in the NEU and DEN. Heavily carbonate cemented layers have high AC and are shaded blue. Right-hand panel shows fluid pressure, expressed as overpressure relative to a hydrostatic gradient. Dashed green lines are possible oil gradients. The exact position of the pressure barrier is uncertain, but the pink box illustrates the likely depth range in which it occurs. Core was available for 3370-3480m; sampled locations shown as circles with sample numbers.**

## 2.2 Pressure data

Pressure data from the sampled well show upwards-increasing overpressure relative to a hydrostatic gradient related to the buoyancy of oil (Figure 2). The data follow straight lines that are interpreted as oil gradients, the slope of which relate to the oil density. Common gradients exist within H5 and within H1-2, but with a significant (2 bar) pressure step between H5 and H2, indicating a barrier to vertical fluid communication in the oil somewhere within a ~25m interval. The lack of pressure measurements in this interval means that it is not possible from pressure alone to determine precisely where the barrier is and what geological feature is responsible, for example the shales and coal interval at the top of H4, any of the numerous shales and coals in H3, or a combination of these. This is further investigated herein.

## 2.3 Carbonate cementation

Published work on carbonate cementation in the Hugin Formation in the Langfjellet area is sparse; some work on diagenesis in rocks that are broadly equivalent stratigraphically was reported by Greenwood et al. (1994). There are several intervals with extensive carbonate cement in the Hugin formation that are clearly evident in the well acoustic logs (Figure 2) and the sampled core (Figure 3). The most prominent of these, up to 2 m thick, are in the H1 zone. There is no clear indication of a significant pressure step across them (Figure 2). Whether these could behave as barriers or baffles is further investigated in this paper.

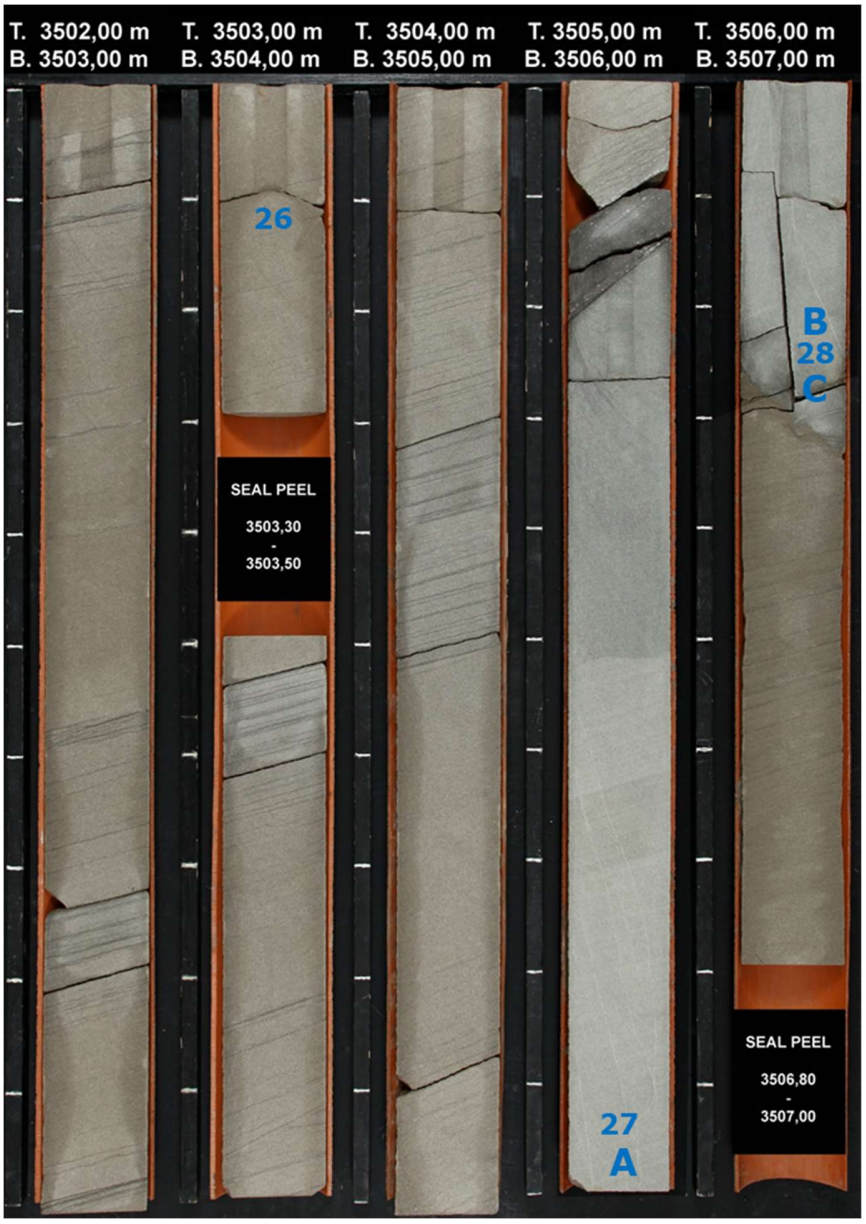


**Figure 3. Core photos from well 25/2-18 ST2, 3502-3507m core depth (3439.1-3444m TVDSS). Numbered sample locations for isotope analysis shown (Table 1). Letters refer to samples available for petrographic study. A heavily carbonate cemented zone with curved boundaries occurs between 3505.2 and 3506.3 m. Above this, carbonate cement is present disseminated in smaller amounts. Faint sub-vertical white traces in the 3505.6-3506.3 m depth range are thin calcite-filled veins.**

# 3. Methods

## 3.1 Sampling and Sample preparation

Thirty-nine samples (Figure 2) were collected from the core of well 25/2-18 ST2 held by the Norwegian Petroleum Directorate. All of the samples were run through a combined residual salt and carbonate extraction protocol as described below. Of these, 33 samples with low or moderate carbonate cement content (<10%) yielded results for formation water $^{87}Sr/^{86}Sr$ using the residual salt analysis (Sr RSA) method, while 6 samples with high carbonate content did not contain sufficient pore salts to yield a meaningful analysis. Sufficient carbonate for successful C and O isotope analysis was present in 31 samples. Of these, 23 yielded sufficient Sr for carbonate Sr isotope analysis. Three samples were available for petrographic work, all from the heavily carbonate-cemented interval at ~3506 m core depth (~3442 m true vertical depth subsea, TVDSS, samples A-C on Figure 3).

Residual salt extraction for Sr isotopes. Samples were selected from core with a strategy to ensure samples were taken either side of any potential flow barriers, and otherwise at regular depth intervals. Samples of ~2 $cm^3$ in volume were taken from near the centre of the core to minimize the risk of contamination by drilling mud. Since oil-based mud was used in this well, formation water contamination from mud fluid was unlikely to be significant in any case. The samples were subsequently gently disaggregated in a mortar and homogenized. The samples were then washed in de-ionized water and left to stand for 10 minutes, then shaken and left to stand for a further 10 minutes. The solution containing water-soluble salts was removed, filtered, acidified

with 2 M $HNO_3$ and passed through an ion exchange column for separation of Sr from other elements, prior to isotope ratio analysis.

Carbonate extraction for Sr isotopes. The solid material remaining after residual salt extraction was rinsed several more times with Milli-Q water to ensure no residual water-soluble salts persisted, with the particulate matter allowed to sediment between each rinse to minimize particle loss. Subsequently, each sample was washed with 0.1M HCl and left to stand for 5 minutes, shaken, and left to stand for a further 5 minutes. The solution containing Sr from the dissolved carbonate fraction was removed, evaporated to dryness and reconstituted in 2 M $HNO_3$ before being passed through an ion exchange column for separation of Sr from other elements.

### 3.2 Petrographic analysis

To investigate carbonate cementation mechanisms, the 3 samples A-C (Figure 3) were studied in the scanning electron microscope (SEM) focusing on mineral composition and micro-texture. The SEM work and image analysis were performed at University of Oslo using methods described in Torabi et al. (2007) and Skurtveit et al. (2015).

### 3.3 Sr isotope analyses

Strontium isotopes were measured on RSA extracts to determine the $^{87}Sr/^{86}Sr$ of present-day formation water and in carbonates to determine the $^{87}Sr/^{86}Sr$ of the water from which they precipitated. Measurements were performed on a Neptune Plus MC-ICP-MS system from Thermo Scientific. The $^{87}Sr/^{86}Sr$ ratio was corrected for mass fractionation by normalizing to $^{88}Sr/^{86}Sr = 8.375209$, and for $^{87}Rb$ by measuring $^{85}Rb$ and using $^{85}Rb/^{87}Rb = 2.592310$. Repeated measurements of the SRM 987 standard at

the time of analysis (inter-day average) yielded $^{87}Sr/^{86}Sr$ of 0.710260 ± 0.000032 (2 SD). Inter-day variations were accounted for by using the daily SRM 987 measured value and normalizing results to its accepted value of 0.71024.

### 3.4 $\delta^{13}C$ and $\delta^{18}O$ isotope analysis of carbonate

Carbonate samples were analysed for C and O isotopes to investigate the origin of the carbon incorporated into the cement (C), and the temperature of cementation (O). After crushing and homogenizing in an agate mortar, an aliquot of resulting powder was heated to 400°C for 4 hours to eliminate any organic carbon. About 100 µg of the aliquot was transferred to a 10 ml vacuum container, placed in a temperature-controlled aluminium block and flushed with helium for 7 min. 0.1 ml 100% $H_3PO_4$ was added and the reaction was controlled at 70°C for 2 hours. The produced $CO_2$ gas was then transferred in a helium carrier gas to a Poraplot Q GC column and onwards into a Thermo Delta V Isotope Ratio Mass Spectrometer (IRMS) for isotope ratio determination.

Repeated analyses of IAEA-CO-1 reference material gives a reproducibility of $\delta^{13}C$ values better than 0.15 ‰ VPDB (2 SD) and of $\delta^{18}O$ values better than 0.30 ‰ VPDB (2 SD). All results are corrected for drift, non-linearity and scale stretching within each batch of analyses. In-house standards were run together with the samples for quality control.

All carbonate carbon and oxygen isotope values are with reference to the VPDB standard. All water oxygen isotope values refer to the VSMOW standard.

### 3.5 Calculation of carbonate precipitation temperatures

Oxygen isotopes in calcite were converted to precipitation temperature using the equation of Kim & O'Neil (1997), after converting calcite $\delta^{18}O$ on the VPDB scale to VSMOW using the equation of Coplen et al. (1983), such that:

$$T(°C) = 18030/\left[1000Ln\left(\frac{(1000+(1.03091\ \delta cc+30.91)}{1000+\ \delta water}\right)+32.17\right]-\ 273.15 \quad \text{Equation 1}$$

Where $\delta cc$ is the $\delta^{18}O$ of carbonate on the VPDB scale, and $\delta water$ is the $\delta^{18}O$ of water on the VSMOW scale. Precipitation from contemporary Jurassic seawater ($\delta^{18}O$ = -1 ‰VSMOW) was assumed, taking the value for pre-glacial conditions from Shackleton & Kennett (1975). The validity of this assumption is tested in the Discussion.

## 4. Results

### 4.1 Characterization of carbonate cements

The 3 studied samples (A-C, Figure 3) from the heavily-cemented zone at ~3442 m TVDSS (Figure 2) all have high carbonate cement content of 38-41 %. Detrital minerals are dominated by quartz, K-feldspar and albite, with some pyrite, rutile, apatite and clay minerals. The detrital grains are observed "floating" within carbonate cement (Figure 4), in that most grains are surrounded by carbonate cement on all sides with very few grain-grain contacts points. The carbonate cement is dominated by calcite with some

minor ankerite observed. Sample porosity is <4 %, with some very small primary pores between grains, and some secondary porosity within dissolving grains.

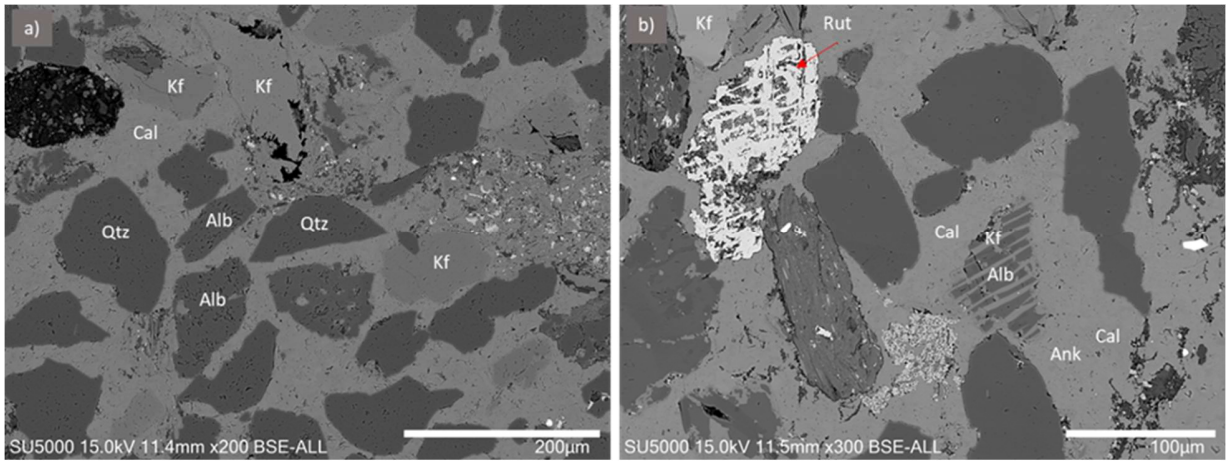


**Figure 4. Back-scattered electron (BSE) SEM images of the heavily carbonate cemented layer in sample A (Figure 3), showing grains of detrital quartz (Qtz), K-feldspar (Kf) and albite (Alb) floating in a cement matrix of calcite (Cal) with some minor ankerite (Ank). Rutile (Rut) is also present. Porosity appears black and is very low. Two separate fields of view. Note slightly different magnification.**

The high carbonate cement contents lead to very high intergranular volumes of ~40%, suggesting that at least some cement formed prior to significant compaction of the sandstones, creating a rigid framework that protected against subsequent compaction during burial. Comparison of an intergranular volume of 40% with compaction curves for quartz-rich sands and an initial porosity of 45% (at zero burial depth) indicate a cementation depth of 300-500 m using the equations of Gluyas and Cade (1997) and Ramm (1992). Such pre-compactional cement is usually interpreted to have a very early (shallow) origin, although early-formed cement can also be recrystallized later (Worden et al., 2019).

Within the calcite cemented sandstone a series of thin calcite-filled veins were observed (Figure 3). Figure 5 shows a SEM image of one of these. Calcite cement fills a cross-

cutting brittle fracture along which detrital grains have been fragmented. This indicates that the fracture must have occurred in rock that was already lithified by calcite cementation, so the vein calcite must be later than at least some of the surrounding cement. The calcite vein might represent a second and later calcite cementation episode, although the lack of discernible difference in composition between the calcite in the vein and the matrix could indicate that it is only slightly later and part of the same overall early cementation process.

To summarize, there is strong petrographic evidence that some of the carbonate cement is very early, pre-compaction, and there are indications of some later carbonate cement.

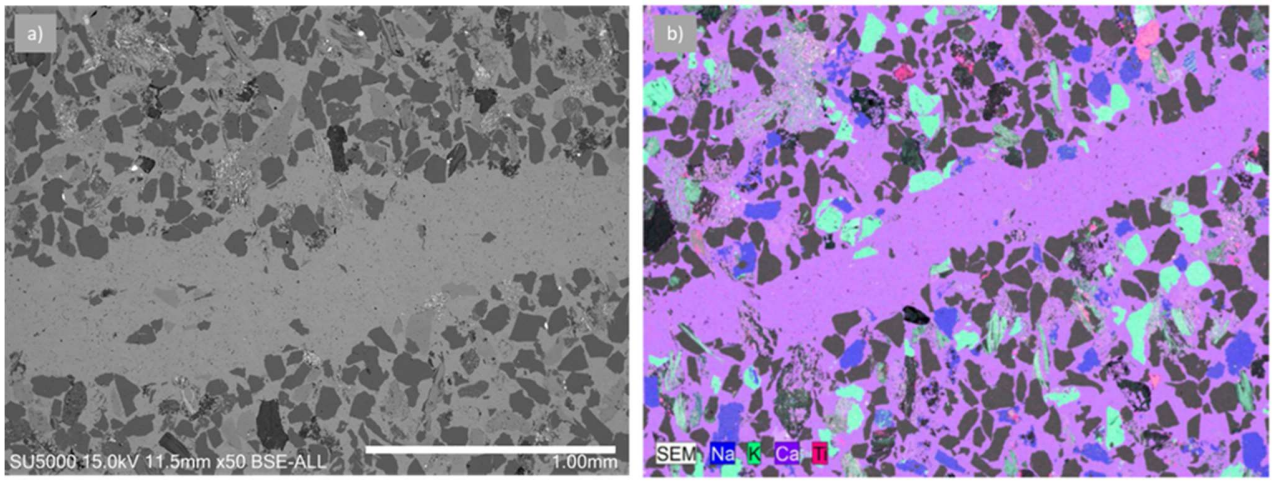


**Figure 5. Backscatter image (a) and element map (b) of a carbonate-filled vein cross-cutting early cement in the heavily carbonate cemented layer in sample A (Figure 3). Plotted elements are Na, K, Ca and Ti. The fracture-filling calcite cement has similar composition to the host rock cement. Note, these are two separate fields of view. Magnification is the same.**

### 4.2 Formation water Sr isotopes

Sr Residual Salt Analysis (RSA) data for well 25/2-18 ST2 (Table 1, Figure 6) reflect the $^{87}Sr/^{86}Sr$ composition of the current formation water at each sampled location in the well. The very constant $^{87}Sr/^{86}Sr$ versus depth over wide depth intervals (3374-3394 m and 3410-3480 m TVDSS) confirms that the samples are not likely to have been significantly contaminated with drilling fluid, as this would have led to erratic variations with depth (Mearns & McBride, 1999). All of the formation water $^{87}Sr/^{86}Sr$ values (0.7099-0.7137) are much higher than the seawater in which these rocks were deposited during the Bathonian to early Oxfordian (0.7069; McArthur et al., 2001). This indicates that the waters have undergone post-depositional changes involving dissolution of Rb-bearing minerals with elevated $^{87}Sr/^{86}Sr$ values.

**Table 1. Sr RSA and carbonate C, O and Sr data for Langfjellet well 25/2-18 ST2. Both core depth and estimated true vertical depth sub-sea (TVDSS) are given. σ is standard deviation. # is sample number.**

| # | Core Depth | Depth TVDSS | Zone | Sr RSA $^{87}Sr/^{86}Sr$ | 2σ | Carbonate $\delta^{13}C$ | σ | Carbonate $\delta^{18}O$ | σ | Carbonate $^{87}Sr/^{86}Sr$ | 2σ |
|---|---|---|---|---|---|---|---|---|---|---|---|
| | m | m | | | x10$^{-5}$ | ‰ VPDB | | ‰ VSMOW | | | x10$^{-5}$ |
| 1 | 3435.6 | 3373.8 | 5 | 0.70999 | 3 | 0.8 | 0.1 | -5.3 | 0.2 | 0.71001 | 4 |
| 2 | 3437.5 | 3375.7 | 5 | 0.70997 | 6 | | | | | | |
| 3 | 3439.5 | 3377.7 | 5 | 0.70990 | 1 | -6.7 | 0.1 | -11.3 | 0.1 | 0.70982 | 3 |
| 4 | 3441.1 | 3379.2 | 5 | 0.71005 | 2 | -16.1 | 0.1 | -5.0 | 0.1 | 0.71148 | 8 |
| 5 | 3442.2 | 3380.3 | 5 | 0.70984 | 4 | -6.1 | 0.1 | -9.6 | 0.0 | | |
| 6 | 3443.5 | 3381.6 | 5 | 0.71008 | 1 | | | | | | |
| 7 | 3450.7 | 3388.7 | 5 | 0.70992 | 4 | -6.4 | 0.1 | -11.0 | 0.0 | 0.70999 | 5 |
| 8 | 3456.4 | 3394.2 | 5 | 0.71004 | 1 | 1.8 | 0.0 | -5.4 | 0.0 | | |
| 9 | 3458.5 | 3396.3 | 4 | 0.71370 | 1 | -2.1 | 0.1 | -7.9 | 0.1 | | |
| 10 | 3462.4 | 3400.1 | 4 | 0.71361 | 1 | -2.0 | 0.1 | -7.7 | 0.1 | | |
| 11 | 3469.5 | 3407.2 | 3 | 0.71287 | 3 | | | | | | |
| 12 | 3471.4 | 3409.0 | 3 | 0.71298 | 7 | 1.6 | 0.1 | -5.9 | 0.1 | | |
| 13 | 3472.1 | 3409.7 | 3 | 0.71309 | 3 | -7.4 | 0.1 | -11.1 | 0.1 | 0.71302 | 4 |
| 14 | 3473.8 | 3411.4 | 3 | 0.71278 | 1 | | | | | | |
| 15 | 3474.6 | 3412.2 | 2 | 0.71309 | 6 | -0.2 | 0.1 | -7.7 | 0.1 | | |
| 16 | 3475.3 | 3412.9 | 2 | 0.71327 | 2 | -7.7 | 0.1 | -13.0 | 0.2 | 0.71321 | 3 |
| 17 | 3476.4 | 3414.0 | 2 | 0.71313 | 1 | | | | | | |
| 18 | 3477.4 | 3414.9 | 2 | 0.71333 | 3 | -6.8 | 0.1 | -10.8 | 0.1 | | |
| 19 | 3480.4 | 3417.9 | 2 | 0.71314 | 3 | | | | | | |
| 20 | 3485.4 | 3422.8 | 2 | 0.71319 | 6 | -3.6 | 0.1 | -8.2 | 0.1 | | |
| 21 | 3488.0 | 3425.3 | 1 | 0.71322 | 4 | 0.2 | 0.1 | -8.7 | 0.1 | 0.71321 | 4 |
| 22 | 3489.3 | 3426.7 | 1 | 0.71310 | 6 | -6.0 | 0.1 | -13.1 | 0.2 | 0.71312 | 2 |
| 23 | 3491.1 | 3428.4 | 1 | | | -5.8 | 0.1 | -10.3 | 0.1 | 0.71203 | 2 |
| 24 | 3493.4 | 3430.6 | 1 | | | -2.8 | 0.1 | -9.0 | 0.0 | 0.71294 | 2 |
| 25 | 3495.2 | 3432.4 | 1 | 0.71320 | 2 | -1.6 | 0.3 | -11.9 | 0.1 | 0.71320 | 5 |
| 26 | 3503.1 | 3440.2 | 1 | | | -2.0 | 0.1 | -10.6 | 0.2 | 0.71315 | 2 |
| 27 | 3506.0 | 3443.0 | 1 | | | -3.4 | 0.1 | -10.7 | 0.1 | 0.71252 | 1 |
| 28 | 3506.3 | 3443.3 | 1 | | | -4.1 | 0.1 | -9.4 | 0.1 | 0.71315 | 3 |
| 29 | 3507.8 | 3444.9 | 1 | 0.71321 | 3 | 0.1 | 0.2 | -7.0 | 0.2 | 0.71316 | 6 |
| 30 | 3511.2 | 3448.2 | 1 | | | -2.2 | 0.1 | -10.7 | 0.1 | 0.71233 | 2 |
| 31 | 3516.5 | 3453.4 | 1 | 0.71320 | 3 | -0.8 | 0.2 | -6.8 | 0.1 | 0.71315 | 8 |
| 32 | 3522.8 | 3459.6 | 1 | 0.71311 | 5 | -3.1 | 0.1 | -8.9 | 0.2 | 0.71298 | 3 |
| 33 | 3524.1 | 3460.9 | 1 | 0.71322 | 4 | | | | | | |
| 34 | 3527.7 | 3464.4 | 1 | 0.71317 | 7 | | | | | | |
| 35 | 3528.1 | 3464.8 | 1 | 0.71338 | 4 | 4.8 | 0.1 | -4.3 | 0.2 | 0.71335 | 5 |
| 36 | 3531.6 | 3468.2 | 1 | 0.71319 | 3 | -5.5 | 0.1 | -10.5 | 0.1 | 0.71343 | 5 |
| 37 | 3534.9 | 3471.4 | 1 | 0.71326 | 2 | -1.0 | 0.1 | -6.7 | 0.1 | 0.71321 | 5 |
| 38 | 3538.5 | 3475.0 | 1 | 0.71317 | 2 | -5.0 | 0.1 | -9.4 | 0.0 | 0.71302 | 3 |
| 39 | 3542.5 | 3479.0 | 1 | 0.71317 | 3 | -5.0 | 0.1 | -10.5 | 0.2 | 0.71311 | 2 |

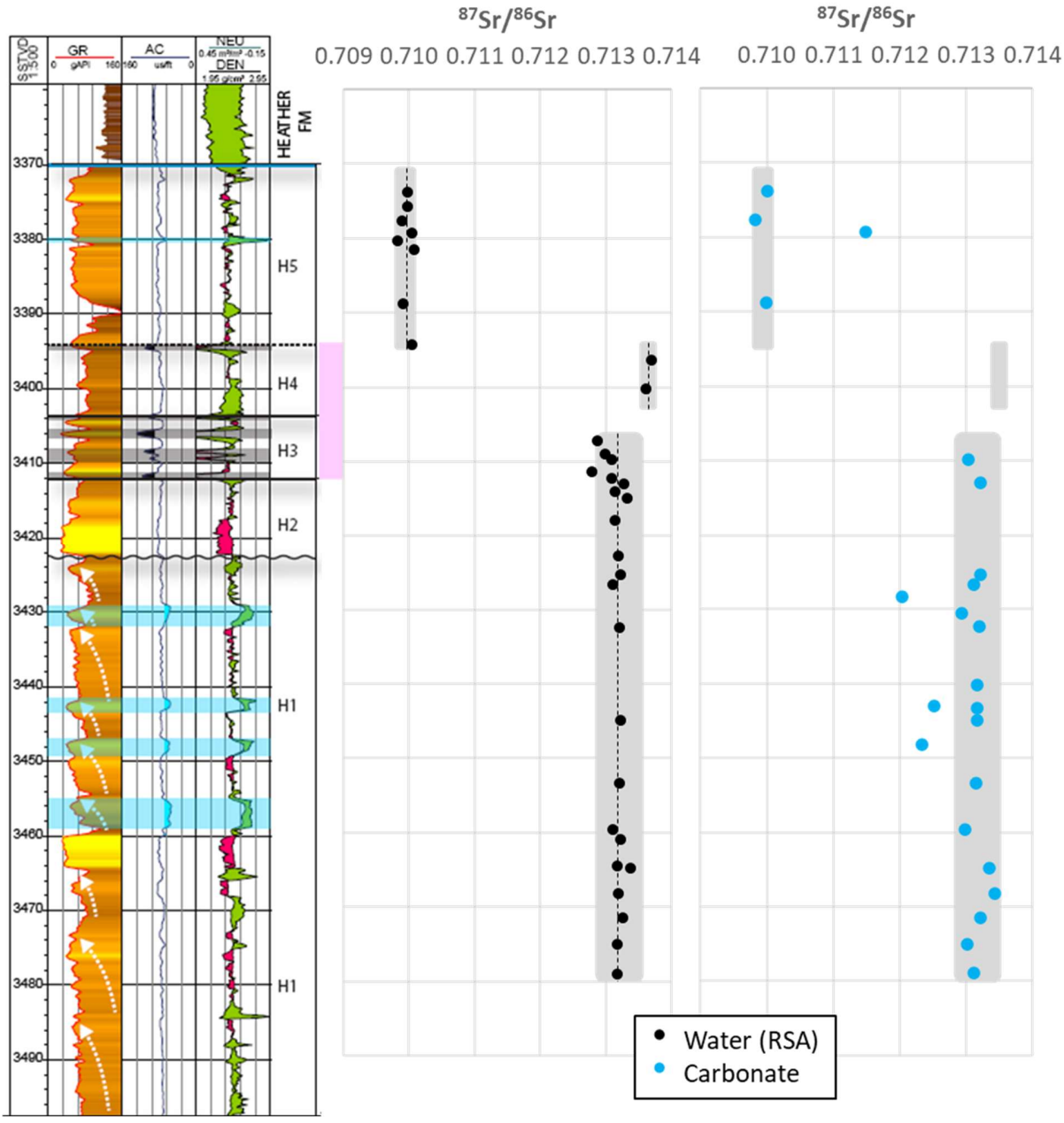


371

372 **Figure 6. $^{87}Sr/^{86}Sr$ ratio of (left) formation water from residual salt analysis and (right) carbonate cements**
373 **versus depth in well 25/2-18 ST2, compared to the well stratigraphy and well log shown and explained in**
374 **Fig. 2. The analytical reproducibility is less than the size of the symbol. Vertical dashed lines in the water**
375 **data show mean $^{87}Sr/^{86}Sr$ values for zones H1-3, H4 and H5 derived from the RSA data, and grey boxes show**
376 **the ± 2σ ranges. The same ranges are shown by the grey boxes superimposed on the carbonate data. Pink**
377 **box shows possible depth range within which the pressure barrier could occur (see Fig. 2).**

378 The Sr RSA data show significant and systematic variations in formation water

379 composition with depth (Figure 6), relating to the Hugin zonal subdivision. For reference

the depths of the zone boundaries in TVDSS/core depth are: base H5 3394.3/3456.45 m, base H4 3394.0/3465.65 m, base H3 3412.1/3474.6 m, base H2 3422.8/3485.4 m. The $^{87}Sr/^{86}Sr$ pattern can be divided into three segments:

1. In the H5 zone, the $^{87}Sr/^{86}Sr$ ratio stays constant at about 0.710 (average 0.70997, standard deviation $\sigma = 0.00008$).
2. In zones H1-H3 $^{87}Sr/^{86}Sr$ again has a very constant value at about 0.713 (average 0.71315, $\sigma = 0.00013$).
3. Between these, in zone H4, two Sr RSA samples have $^{87}Sr/^{86}Sr$ averaging 0.71366 ($\sigma = 0.00006$).

The consistency of $^{87}Sr/^{86}Sr$ values in each zone are shown by grey shading on Figure 6, representing ± 2 σ ranges.

The homogeneity within each of these depth intervals could indicate a lack of any significant internal barriers to vertical Sr mixing. There is, however, a small but significant (3.8 σ) step between zones H3 and H4, and a highly significant step change (44 σ) in $^{87}Sr/^{86}Sr$ at the top of zone H4. Such a clear steps in water composition, particularly the top-H4 step, is strong evidence for lack of formation water mixing between the reservoirs above and below the step over a geological timescale (Smalley et al., 2020). The implications for degree of hydraulic communication and barrier strength are addressed in the Discussion.

### 4.3 Carbonate Sr isotopes

Samples containing carbonate cement were analysed for carbonate $^{87}Sr/^{86}Sr$ ratio to determine the Sr isotopic composition of the water from which the carbonates

403 precipitated, and how they compared to the current formation water compositions
404 derived from the RSA data. The results are given in Table 1 and plotted on Figure 6.
405 The carbonate data form two populations, one in Hugin zone H5 (mean = 0.71033, σ =
406 0.00077), which is indistinguishable from the H5 RSA-derived current water $^{87}Sr/^{86}Sr$
407 values (mean = 0.70997), and a second in zones H1-3 (mean = 0.71302, σ = 0.00035),
408 which is indistinguishable from the H1-3 RSA-derived current water $^{87}Sr/^{86}Sr$ value
409 mean of 0.71315. No carbonate was present in the H4 samples. The carbonate
410 $^{87}Sr/^{86}Sr$ data thus follow same pattern as the formation water, with similar values in H5
411 and H1-3, and with a distinct step across H4 (Figure 6).

412 Another way of describing the carbonate $^{87}Sr/^{86}Sr$ data is that, in H5, 3 out of the 4
413 carbonate samples plot within the formation water mean ± 2σ range for this zone
414 (Figure 6) and in H1-3, 17 out of the 20 samples plot within the formation water range
415 for these zones. The one sample in H5 that falls on the high side of the baseline
416 (sample #4, 3379.2 m TVDSS) also has unusual C isotopes, discussed later.

417 The $^{87}Sr/^{86}Sr$ in all of the sampled carbonate cements is significantly higher than
418 seawater at the time of deposition and any calcareous fossil material formed therefrom
419 (0.7069; McArthur et al., 2001). Some water-rock interaction including Rb-bearing high-
420 $^{87}Sr/^{86}Sr$ minerals must thus already have occurred prior to precipitation of any of these
421 cements. In H1, three samples that are highly cemented have carbonate Sr isotope
422 analyses but no corresponding Sr RSA data, due to their very low porosity and hence
423 negligible residual salts to extract. These samples all have low $^{87}Sr/^{86}Sr$ (Figure 6).
424 This indicates that at least some carbonate cementation began before the current water
425 $^{87}Sr/^{86}Sr$ compositions were established.

### 4.4 Carbonate C and O isotopes

The samples analysed for $\delta^{13}C$ and $\delta^{18}O$ were spread across the entire H1-3 and H5 intervals, including the thick heavily carbonate cemented intervals shown on Figure 2 and Figure 3, as well as several thinner zones and rocks containing smaller amounts of disseminated carbonate cement (e.g., sample #26 on Figure 3).

The carbonate carbon and oxygen isotope data are shown in Table 1 and plotted on Figure 7. This figure also shows an interpretation of carbonate $\delta^{18}O$ in terms of precipitation temperature (see Methods for details), assuming precipitation from contemporary Jurassic seawater (see Discussion).

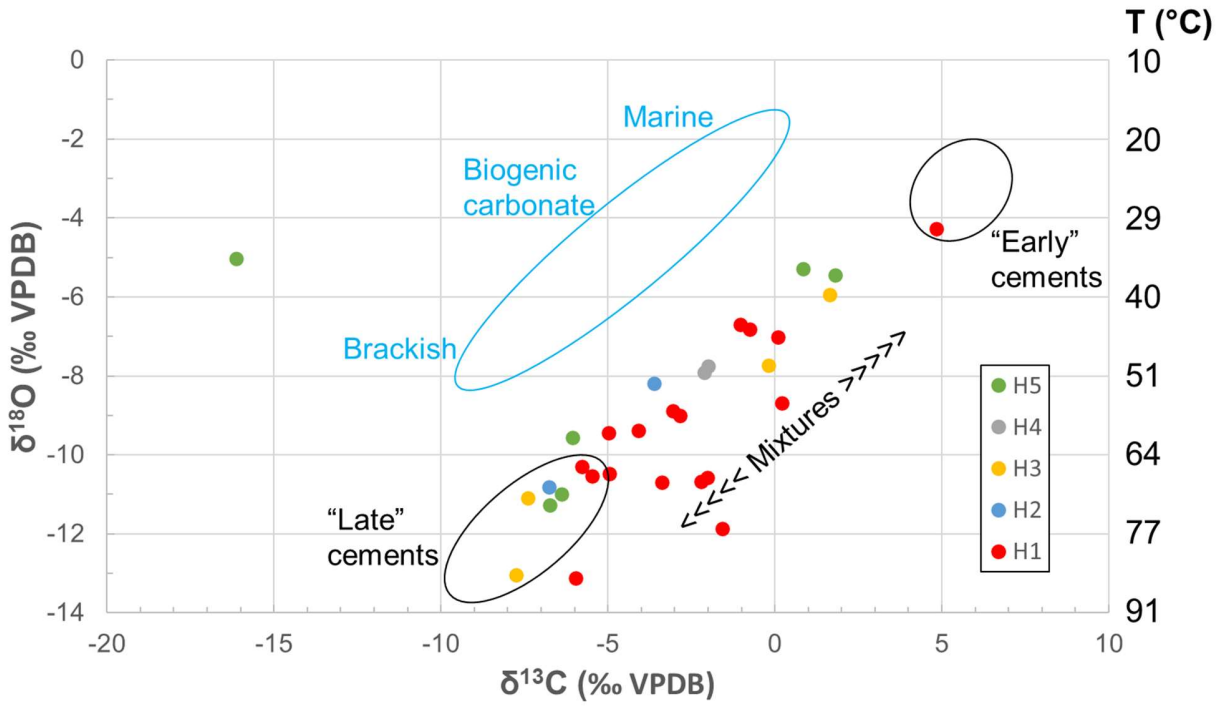


**Figure 7. Carbon and oxygen isotope data for the analysed samples, coloured by stratigraphic zone. Potential endmember carbonate compositions are shown. See Methods for explanation of temperature scale, which assumes a Mid Jurassic seawater $\delta^{18}O$ composition. Present reservoir temperature is 116 °C. Range of marine to brackish biogenic carbon compositions from Sampei et al. (2005).**

All of the samples (except one outlier) plot along a positive linear trend. There are two ways to interpret this relation:

1. The carbonate cements precipitated over a range of temperatures (and/or formation water $\delta^{18}O$ compositions) and, for some reason or through coincidence, as the rocks were progressively buried and temperature increased (and/or formation water composition changed), the isotopic composition of carbon has varied at the same rate.
2. The samples contain physical mixtures of two generations of cements in varying proportions each with a roughly constant composition (shown by the endmembers on Figure 7).

It is difficult to conceive of a process that could have caused the linear relation in the case of alternative (1). There are various processes than can affect the $\delta^{13}C$ of precipitating carbonate (Irwin et al., 1977), such as dissolution of pre-existing biogenic carbonate ($\delta^{13}C \approx 0$ ‰ if dominated by marine compositions, Figure 7), oxidation of organic matter ($\delta^{13}C < -20$ ‰), bacterial methanogenesis ($\delta^{13}C > +5$ ‰), bacterial sulphate reduction ($\delta^{13}C < -25$ ‰) or thermal decarboxylation ($\delta^{13}C < -20$ ‰). These processes operate under strict physical conditions: for example, aerobic oxidation of organic matter requires an oxidizing environment very close to the sediment water interface; bacterial methanogenesis and sulphate reduction require optimal temperatures for the relevant bacteria to thrive, and thermal decarboxylation requires burial temperatures hot enough to degrade organic material. These thresholds for the various processes mean that, during progressive burial and heating of a rock, the processes will be switched on and off at various times. Given these factors, it is extremely unlikely that the carbon

464 produced by these various processes could produce a constant gradual change in the
465 $\delta^{13}C$ of precipitating carbonate that almost exactly balances the increasing temperature
466 documented by the $\delta^{18}O$, so as to produce the linear relation in Figure 7.

467 The second explanation is thus more likely, involving fewer assumptions, and being
468 supported by the petrographic evidence for early pre-compaction cement and at least
469 one generation of later cement. Other detailed studies of C and O isotopes in carbonate
470 cements have come to a similar conclusion to explain co-linearity of the data (Klein et
471 al., 1999). We thus propose that there are at least two distinct generations of carbonate
472 cements that precipitated at different times, each with $\delta^{13}C$ compositions characteristic
473 of the dominant carbon source at the time. These cement generations form
474 endmembers that are situated at or slightly beyond each end of the linear trend on
475 Figure 7. The different cement generations are closely mixed at the sample scale due to
476 the process of late cement nucleation on existing early cement and later cement filling
477 of fractures cutting through earlier cement (Figure 5). Consequently, each sample (each
478 data point on Figure 7) contains a physical mixture of both endmember cements in
479 various proportions. The linear relation in Figure 7 then simply reflects the proportion of
480 each cement type in each sample. The lower temperature end of the trend contains
481 relatively higher proportions of the early cement endmember, and the higher
482 temperature end of the trend contains samples with relatively more of the late cement
483 endmember. Note that, with this explanation, the temperatures of precipitation of the
484 endmembers are valid, but the temperatures calculated for intermediate mixtures are
485 meaningless, as no cement actually precipitated at those “mixed” temperatures. The
486 two endmembers are further discussed below.

Note that the mixing trend does not indicate any significant involvement of biogenic carbonate fossil material, which would plot above the observed trend, the exact position depending on the balance of marine versus freshwater input (Figure 7). Mixtures of biogenic carbonate with two cement types would plot within a roughly triangular area, the shape of which would depend on the composition of the biogenic material; this is not seen. Given the lack of evidence for carbonate bioclastic material in the samples, and the likely C-O isotopic composition of such material (Figure 7), it is unlikely that bioclasts are involved in the physical mixture of carbonate types.

The one outlier on Figure 7, sample #4 from 3379.2m TVDSS, has one of the highest $\delta^{18}O$ values (-5 ‰), indicating a low precipitation temperature; it also has the lowest $\delta^{13}C$ (-16 ‰). This sample could possibly contain some very early cement formed in the sulphate reduction zone, with carbon derived from oxidation of local organic material. This sample also has a high $^{87}Sr/^{86}Sr$ compared to other H5 carbonates (Figure 7); this cement could thus have formed closer to the sediment-water interface in the sulphate reduction zone, possibly before the homogeneous H5 formation water $^{87}Sr/^{86}Sr$ composition was established.

# 5. Discussion

## 5.1 Timing of carbonate cements

### Thermal modelling

To estimate the timing of the carbonate cements, it is necessary to reconstruct the thermal history of the rocks, so that the interpreted oxygen isotope temperatures (Figure 7) can be converted into time and burial depth. In this case, there are some specific

challenges. Modelling thermal evolution in sedimentary basins involves understanding the relevant full-lithospheric processes and thermal effects of force and energy balances (Hartz et al., 2017; Rüpke et al., 2013; Wangen, 2010). The use of basin modelling in the petroleum industry usually focuses on predicting the thermal maturation of kerogen to generate oil and gas, which generally occurs at elevated temperatures. In the present case, however, it is the cooler part of the thermal history that is relevant for the early cements. Scoping analysis using finite element models of multistage rifting (software: Mira by Bergwerk) and a non-transient thermal model (Souche et al., 2017) revealed that the early heating of the Mid Jurassic rocks above 30°C (when the early cement was precipitated) is mostly controlled by the temperature at the sediment water interface.

Seawater temperature in the Jurassic is a topic of debate, and may have fluctuated significantly (Korte et al., 2015), but there is a consensus that that the Mid Jurassic waters in what is now the North Sea were much warmer than today (Royer et al., 2004). Using Hantschel and Kauerauf's (2009) temperature estimates based on latitude, the Mid Jurassic surface waters at Langfjellet (~40°N) had mean annual temperatures of ~26°C. The Sleipner-Hugin sediment package included continental and shoreface sediments deposited in very shallow waters, so surface water temperatures can also be applied to the sediment water interface. The overlying Heather and Draupne Formations were deposited in deeper water deposits, but water temperature was increasing, and the sediment water interface temperature is estimated to remain constant at 26°C. The resulting burial and thermal histories are shown in Figure 8.

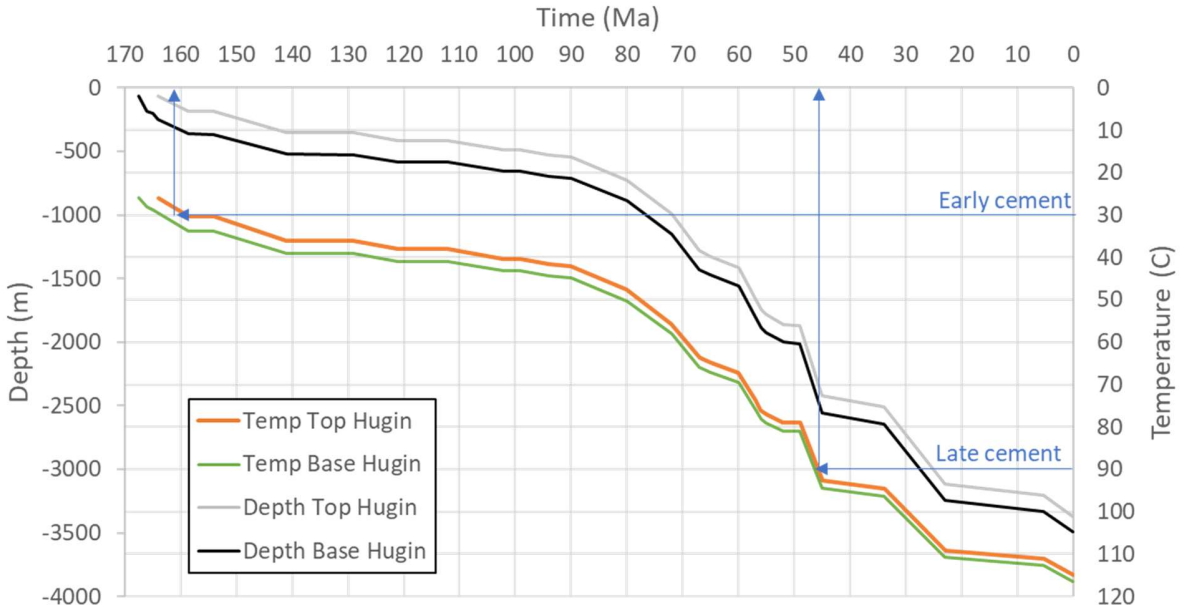


**Figure 8. Burial and thermal history for the Hugin reservoir in the studied well. The thermal model assumes a Mid to Late Jurassic mean annual temperature at the sediment-water interface of 26°C. Note that the entire sedimentary column was modelled but only the top and base of the Hugin is illustrated here. Average current reservoir temperature is 116°C. Conversion of O isotope-derived temperatures to time and depth is illustrated by the arrows.**

**Assumed formation water $\delta^{18}O$ value**

The carbonate precipitation temperatures shown on (Figure 8) are based on the assumption that the sediments were deposited in water with a contemporary Jurassic seawater composition ($\delta^{18}O$ = -1 ‰SMOW, after Shackleton & Kennett,1975), and that this water composition persisted throughout the cementation history. This section addresses uncertainties in this assumption.

**Formation water composition during deposition**.

The assumption of an initial seawater composition is safe for the sand-dominated shallow marine and shoreface deposits in Hugin zones H1,2,4 and 5 (Figure 2), as these would have been deposited in water well-connected to the open sea. For zone 3, deposited in a coastal plain setting, the initial water composition is less certain. The

549 initial water $\delta^{18}O$ composition could have been isotopically lighter if there was significant
550 input from meteoric waters (e.g., river systems). The $\delta^{18}O$ composition of meteoric
551 water is dependent on latitude and average surface temperature (Fricke & O'Neil,
552 1999). Based on the estimated Mid Jurassic mean annual temperatures of ~26°C in the
553 Langfjellet area discussed earlier, pure meteoric water would be expected to have a
554 $\delta^{18}O$ of about -5 ‰, and mixtures of meteoric water and seawater would have $\delta^{18}O$
555 between -1 and -5 ‰. However, a water $\delta^{18}O$ of <-2 ‰ would lead to a calculated
556 precipitation temperature for the earliest carbonate cement lower than the presumed
557 ambient temperature of ~26°C during deposition. We thus consider it unlikely that the
558 initial water composition was significantly lower than -1 ‰.

559 It is possible in a coastal plain setting for evaporation to lead to heavier oxygen isotope
560 compositions in the remaining water; for example Barrie et al. (2015) saw $\delta^{18}O$
561 increases of ~4 ‰ due to evaporation in an estuary after large amounts of evaporation
562 (40%). Under more reasonable amounts of evaporation, increases in $\delta^{18}O$ are likely to
563 be small and, if anything, will counteract the effects of any isotopically lighter meteoric
564 water involvement. There is thus no compelling reason to change the assumption of an
565 initial water composition of -1 ‰, though recognising there is some uncertainty. We note
566 too that the same full range of carbonate cement $\delta^{18}O$ values is exhibited by samples
567 from zones H1, H3 and H5, which supports the assumption that H3 did not have a
568 unique lighter $\delta^{18}O$ composition due to greater meteoric involvement.

569 **Formation water modification during burial**

570 Unfortunately, no oxygen isotope measurements are available of present-day formation
571 water in Langfjellet. Present day formation water composition in North Sea oil fields

generally have been interpreted as mixtures between endmembers consisting of seawater ($\delta^{18}O$ = -1 ‰), brine derived from evaporated seawater ($\delta^{18}O$ up to +8 ‰), and meteoric water ($\delta^{18}O$ = -5 ‰; McCartney and Rein, 2005, and references therein), the former two being primary in that they were trapped in sediments during deposition, the latter being introduced during subsequent uplift and subaerial exposure. While minor amounts of evaporation may have been involved in the Langfjellet zone H3 coastal plain deposits, as discussed above, it is unlikely that highly evolved brines were involved; indeed large brine components are mainly restricted to fields close to thick evaporite deposits (McCartney and Rein, 2005), which is not the case here. The nearest potential source of post-depositional meteoric water influx is the Utsira High, but this about 90 km away and other Mid Jurassic reservoirs in the region do not show strongly negative $\delta^{18}O$ values (for example, Bruce 0‰, Hild +2 ‰, Oseberg -2 ‰; Warren and Smalley, 1994). The compilation of water data for Mid Jurassic reservoirs in the North Viking Graben area by McCartney and Rein (2005) have an average $\delta^{18}O$ value of -1 ‰. Consequently, although uncertainty remains, the assumption of Langfjellet formation water having a $\delta^{18}O$ value of -1 ‰ throughout the carbonate cementation history is reasonable.

**"Early" carbonate endmember**

The highest $\delta^{18}O$ value (Figure 7) is -4 ‰ (about 30°C), although that sample could still contain some of the higher-temperature cement, so this may not represent the pure endmember. The "early" generation of cement thus must have precipitated at or slightly lower than 30°C, assuming a formation water with $\delta^{18}O$ = -1 ‰.

596 The thermal model (Figure 8) suggests that the Hugin Formation was heated to 30°C
597 very soon after deposition. The base of the Hugin reached 30°C at about 164 Ma, some
598 3.5 my after deposition (167.5 Ma), about the time that the top Hugin was being
599 deposited. The top of the Hugin reached 30°C during the deposition of the overlying
600 Heather and Draupne shales. The top of these shales is marked by the super-regional
601 Base Cretaceous Unconformity, marking a ~15 million-year hiatus before the onset of
602 Cretaceous deposition. By this time, the Hugin was at 35-40°C. The average Hugin
603 temperature would have reached 30°C at about 162 Ma. At this time burial depth would
604 have been only a few hundred metres (Figure 8).

605 This relatively shallow origin for the early cement endmember is supported by the
606 petrographic evidence that the early cement is pre-compaction (Figure 4), consistent
607 with precipitation at no more than a few hundred metres depth, and the positive carbon
608 isotope values of this end-member (+3 to +5‰, Figure 7), indicating the involvement of
609 bacterial methanogenesis (Irwin et al., 1977). Although methanogenesis can occur up to
610 ~50°C (Dale et al., 2014) it would not normally occur directly at the sediment-water
611 interface. When marine sediments are progressively buried, they pass through zones of
612 aerobic oxidation (very close to the sediment-water interface) and then a bacterial
613 sulphate reduction process, until the seawater sulphate has been used up (Whiticar,
614 1999). This requires some degree of burial, at least a several tens of metres (Irwin et
615 al., 1977), before bacterial fermentation can then take over and dominate. Note too, that
616 the early cements contain $^{87}Sr/^{86}Sr$ values of 0.710-0.713, much higher than
617 contemporaneous Jurassic seawater (0.7069; McArthur et al., 2001). This indicates that
618 the carbonate was precipitated sufficiently far below the sediment-water interface that

water-rock interaction had come to dominate the Sr budget of the formation water rather than seawater. Overall, the data indicate that the early carbonate cement endmember precipitated at shallow burial depths, probably a few hundred metres below the sediment-water interface, at about 162 Ma.

**“Late” endmember**

The lowest carbonate cement oxygen values are about -13 ‰ (T = ~90°C, Figure 7), but those samples could still contain some low temperature cement, so the high temperature endmember has to be at least 90°C, but could be somewhat higher. Comparison with the thermal history (Figure 8) indicates that the Hugin reservoir reached 90°C at about 46 Ma, when the rocks were buried to a depth of ~2500 m.

This timing of the late cement endmember is consistent with the carbon isotope data. The carbon isotope composition of this endmember has to be <-8 ‰ (Figure 7), and indicates a contribution of carbon from an isotopically lighter source. As the sediments would have passed through the aerobic oxidation and sulphate reduction zones much earlier, prior to precipitation of the early cements, the most likely source of isotopically light carbon at this depth is the thermal decarboxylation of organic material, which starts to become significant at >60°C (Bjørlykke, 2010), corresponding to a depth of >1.3 km in the current study area (Figure 8). The carbon isotope data thus fit with a higher temperature origin for this endmember, possibly related to the onset of oil generation. The combined data indicate a protracted carbonate cementation history, with the later cements being >100 my later than the early cements.

641 **5.2 Influence of carbonate cemented layers: barriers or baffles?**

642 The homogeneous formation water $^{87}Sr/^{86}Sr$ composition in the lower part of the well
643 (~0.7132) is unaffected by the various heavily-carbonate-cemented intervals seen on
644 the log (Figure 6) and sampled from core, and no step changes in $^{87}Sr/^{86}Sr$ are seen
645 across any of them. There is thus no evidence to suggest that the cemented intervals
646 form extensive barriers to vertical fluid movement.

647 To investigate this further, consider a case where, at some time in the past, there had
648 evolved a difference in water $^{87}Sr/^{86}Sr$ above and below one of the carbonate-cemented
649 intervals in H1 (for example the 4 m-thick zone at ~3547 mTVDSS on Figure 6). Using
650 present day temperature (116°C, Figure 8), and representative H1 porosity and water
651 saturation values, an effective diffusion coefficient $D$ for Sr would be about 5.24 x $10^{-5}$
652 $m^2y^{-1}$ using (Go et al., 2014):

$$D = \frac{D_m S_w^n \phi^{m-1}}{\left(1 + \frac{(1-\phi)\rho K_d}{\phi}\right)} \qquad \text{Equation 2}$$

653

654 where $D_m$ is the tracer diffusion coefficient of Sr (7.27 x $10^{-2}$ $m^2y^{-1}$ at 116°C), $S_w$ is the
655 water saturation (0.5), $n$ is the saturation exponent (assumed 2 for water wet rocks), $m$
656 is the cementation factor (2 for sandstone), $\phi$ is porosity (0.18, from well log data), $\rho$ is
657 the density of the rock (2650 kg $m^{-3}$) and $K_d$ is the Sr sorption coefficient (assumed
658 0.005 $m^3$ $kg^{-1}$ for sand).

659 The homogenization time ($t$) by diffusion of Sr isotopes in waters above and below the
660 cemented interval can be estimated using (Smalley et al., 2020):

$$t \approx -\frac{L^2}{\pi^2 D} \ln\left\{\frac{\pi \Delta c}{2|c_1 - c_0| \sin\left(\frac{\pi l}{L}\right)}\right\}$$ Equation 3

where $L$ is the Length of the reservoir interval, $l$ is the distance above the base where the initial step in composition occurs (in this case $l = L/2$), and $\Delta c$ is how similar the $^{87}Sr/^{86}Sr$ values must be before they are considered homogenized (assumed here as 0.0001), and $c_0$ and $c_1$ are the initial $^{87}Sr/^{86}Sr$ values above and below the initial compositional step (here assumed as 0.710 and 0.713, equivalent to the H1-3 and H5 average compositions on Figure 6). Assuming that the heavily-cemented zone has negligible diffusional flux *through* it, and that mixing of the waters above and below the cemented zone occurs by mixing in uncemented rock *around* the cemented zone, a step in $^{87}Sr/^{86}Sr$ across a 4-m thick heavily-cemented zone would then take about 0.21 my to homogenize if the cement were a spherical concretion. This would increase to 1.1 my for a 5 m-long layer, 3.3 my for a 10 m layer, 62 my for a 50 m layer and 237 my for a 100 m layer. Consequently, if the carbonate cemented layers had been of significant size, more than a few tens of metres in length, it is likely that any heterogeneities in water $^{87}Sr/^{86}Sr$ that might have existed would have been preserved, and be represented by discontinuities in water $^{87}Sr/^{86}Sr$ across the cemented interval. This is negative evidence, as it is possible that the lack of a discontinuity in water composition across cemented layers is because heterogeneities in water composition never evolved, or were mixed by other processes such as advection before oil was emplaced. Nevertheless, it is clear that water compositional heterogeneities did exist in other parts of the succession (between H1-3, H4 and H5, Figure 6), and thus could have existed within H1 at some time in the past. Combined with the lack of pressure change across the carbonate-cemented intervals (Figure 2), the lack of change in water

composition is taken to indicate that they are not sufficiently long or continuous to have a significant barrier effect, though a minor baffling effect cannot be ruled out.

### 5.3 Where exactly is the pressure barrier and what is it?

The fluid pressure data (Figure 2) show that there are parallel oil pressure gradients in Hugin zone H5 and in H1-3, but with an offset of ~2 bar between them. This natural pressure disequilibrium indicates a significant barrier to fluid flow (i.e., oil flow, as oil is the continuous phase in the reservoir). As an extreme limiting case, the time for pressure to equilibrate in the absence of a barrier over the entire ~100 m depth range ($L$ = 100 m) for which pressure data are available can be estimated using (Smalley et al., 2004):

$$t\ (s) \approx \frac{\text{ø} C \mu L^2}{k} \qquad \text{Equation 4}$$

where $\text{ø}$ is porosity (0.18), $C$ is the effective compressibility (assumed here to be a typical oil-filled reservoir compressibility of 2.5 x $10^{-8}$ $Pa^{-1}$), $\mu$ is oil viscosity (assumed as 1 cP) and $k$ is average permeability, estimated from logs at ~20 mD (2 x $10^{-14}$ $m^2$).

In the absence of a barrier, the pressure would equilibrate by pressure-driven flow to one constant gradient in about 24 days. It is not known how long the pressure step has existed, but it is possible that it arose at the time of oil filling several million years ago. To maintain the pressure discontinuity over such time would demand a very low permeability laterally extensive and continuous barrier. The pressure data do not, however, pinpoint the exact position or cause of the barrier effect, as there is a ~25 m gap in the data (Figure 2). The lowermost pressure point above the discontinuity is in

704 the lowermost part of H5 (3392.9 m TVDSS), while the uppermost pressure point below
705 the discontinuity is in H2 (3415.1 m TVDSS), some 6 m below the base of H3; the
706 barrier could be anywhere between these pressure points (i.e., 3392.1-3415.1 m
707 TVDSS). In the intervening section (Figure 2, Figure 9, Figure 10; please note, depths
708 on Figure 2 are TVDSS, while those on Figure 9 and Figure 10 are core depth), there
709 are thin sands, silts, shales and four coal layers in H3; while H4 includes a ~4 m-thick
710 clayey sand layer, a sandier interval and then a thin organic-rich shale and coal at the
711 top (3393.5 m TVDSS, 3456.5 m core depth); H4 is bounded above by a flooding
712 surface, forming the boundary with H5. Based on pressure data alone, any of these
713 shaley or coaly intervals could potentially form the barrier, either alone or in
714 combination.

715 The water $^{87}Sr/^{86}Sr$ data (Figure 6) help to constrain the barrier position due to the
716 vertical resolution of the RSA sampling method: there are 11 Sr RSA data points within
717 the depth range in which the barrier could occur (samples 8-18, Table 1, Figure 9,
718 Figure 10). Samples 15-18 (Figure 10) are from zone H2, where there are no geological
719 features that could be interpreted as a barrier, and as expected their $^{87}Sr/^{86}Sr$ values lie
720 within the narrow mean ± 2σ range of values from H1 and H2. At the base of H3 is a
721 coal layer (3473.9-3474.5m core depth, Figure 9), and immediately above this, sample
722 14 has a $^{87}Sr/^{86}Sr$ of 0.71278, which lies just below the mean ± 2σ range for H1 and H2
723 (Figure 10). This subtle compositional change could possibly indicate a barrier effect of
724 the base-H3 coal layer. However, sample 13 that is situated only 1.7 m shallower and
725 within the same sand layer has a $^{87}Sr/^{86}Sr$ of 0.71309, very close to the H1/H2 average
726 and the next two samples, sample 12 situated in a thin shale between two coal layers

(3471.55-3471.80, 3470.5-3471.0 m core depth, Figure 9) and sample 11 above these coal layers all fit within the same mean ± 2σ range of $^{87}Sr/^{86}Sr$ values and are indistinguishable from the compositions of the underlying H1-H3 samples (Figure 10). Consequently, there is no compelling case for assigning a barrier effect to any of the coals and shales in the upper part of H2 or the lower part of H3.

There is a change in $^{87}Sr/^{86}Sr$ values between the topmost H3 sample (11, 3407.2 mTVDSS, 3569.5 m core depth, Figure 10) and the lowermost H4 sample (10, 3400.1 mTVDSS, 3462.4 m core depth), which has a $^{87}Sr/^{86}Sr$ value of 0.7136, significantly higher than the mean + 2σ value of 0.7134 of the underlying H1-H3 samples. It is thus possible that a barrier exists in the upper part of H3 or lower part of H4 (3462.4-3469.5 m core depth, 3400.1-3407.2 m TVDSS), for which the coals at 3406 and 3404 mTVDSS (3468, 3465.8 m core depth; Figure 6, Figure 9, Figure 10) and/or the thin shaley layer at (3400-3406 mTVDSS, 3467.5 m core depth) are the main candidates.

The ~1 m-thick organic-rich shale and coal layer at the top of H4 (Figure 9, Figure 10) is overlain by H5 sands at 3394 m TVDSS (3456.4 m core depth). These beds are bracketed tightly by Sr RSA samples 8 and 9 (Figure 10). Sample 9, from ~0.9 m below the shale has a $^{87}Sr/^{86}Sr$ value of 0.71370, similar to sample 10 lower down in H4 (Figure 10). Sample 8 is only a few cm above the coal, from the very base of H5, and this has a $^{87}Sr/^{86}Sr$ value of 0.71004, lying within the tight mean ± 2σ range for zone H5 (Figure 6, Figure 10).

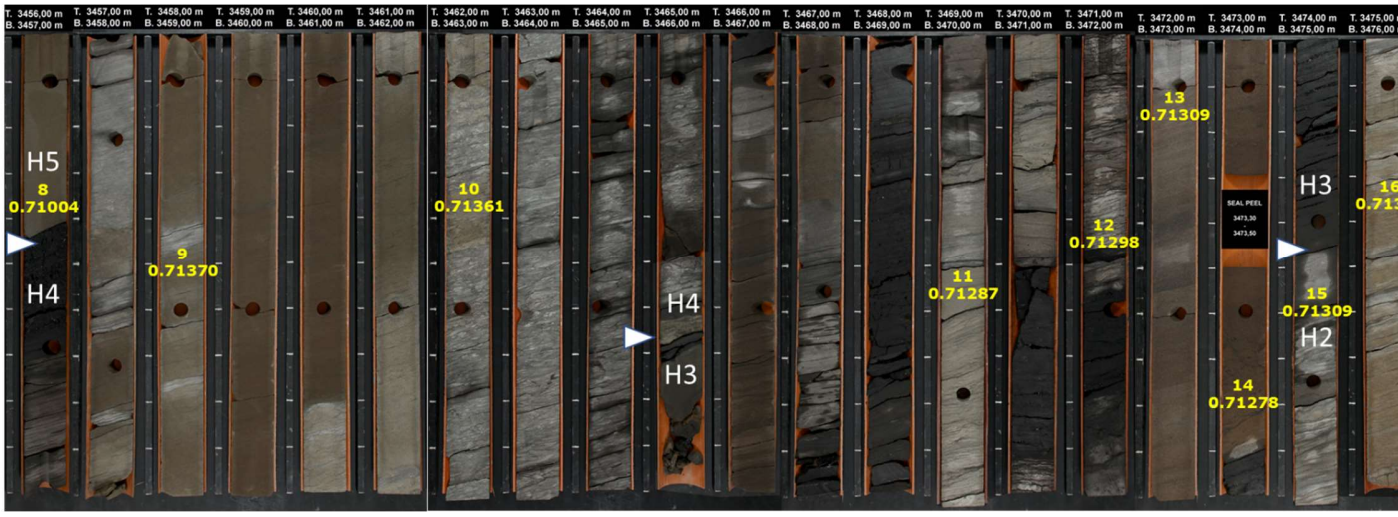


747

748 **Figure 9. Core photograph montage for the interval spanning the pressure barrier (3456-3477 m core depth,**
749 **3393.8-3414.5 m TVDSS). Zone boundaries are shown by white triangles. Yellow numbers represent the**
750 **sample number (Table 1) and Sr RSA $^{87}Sr/^{86}Sr$ measurement at that specific location. The $^{87}Sr/^{86}Sr$ values are**
751 **also plotted above, showing where the steps in water composition occur. The main barrier candidate lies**
752 **between samples 8 and 9. A secondary barrier may exist between samples 10 and 11.**

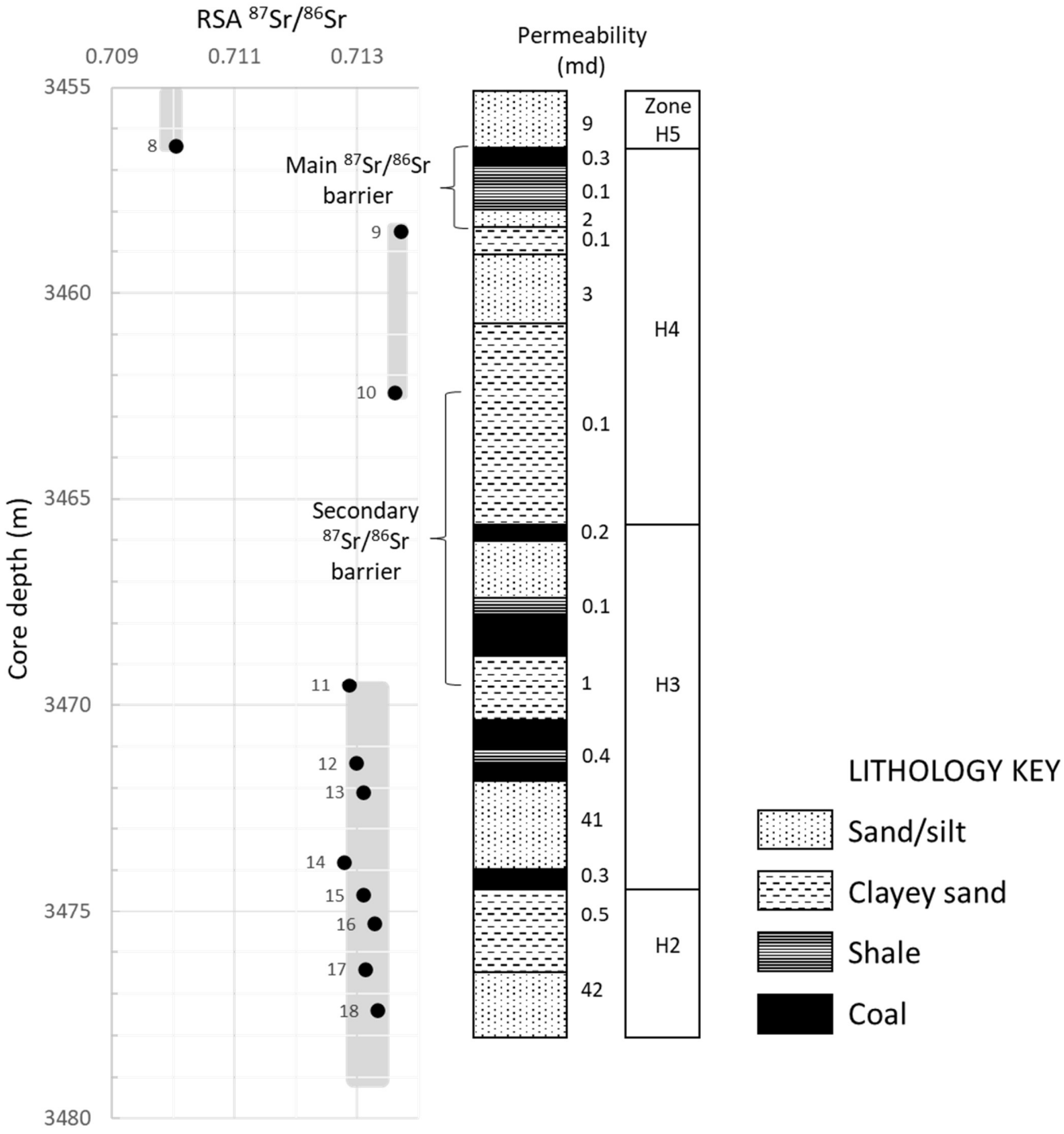


753

754 **Figure 10. Summary of information from core covering the depth interval in which the pressure barrier**
755 **occurs (Figure 2). Depth is core depth (to compare with Figure 9). Reservoir zonation is shown, together with**
756 **summary lithologies from core and representative air permeabilities. The depth intervals are marked in which**
757 **the $^{87}Sr/^{86}Sr$ barriers are situated (Figure 6), which are identified by the steps in RSA $^{87}Sr/^{86}Sr$ between the**
758 **grey shaded ±2σ ranges from Figure 6. The Sr RSA sample numbers are shown (from Table 1).**

This dramatic shift in formation water $^{87}Sr/^{86}Sr$ (44 standard deviations of the H5 data) across a 1.2 m-thick coal and shale interval (3456.45-3457.65 m core depth, 3394.2-3395.4 m TVDSS) indicates this to be the main discontinuity to vertical fluid communication in the Hugin reservoir and the strongest candidate for explaining the observed pressure step (Figure 2).

The significance of the step change in $^{87}Sr/^{86}Sr$ at the top of H4 can be investigated using simple diffusion modelling and some limiting cases using equation 7 of Smalley et al. (2020) to estimate the rapidity with which such a sharp compositional step would become blurred in the absence of a barrier.

Assuming representative Hugin reservoir properties, the observed sharp step change in water composition would begin to be blurred after only 0.1 million years, deviating significantly from the observed Sr RSA pattern. Within 10 million years, the step would disappear and become modified to a smooth gradient.

Could the observed step change in $^{87}Sr/^{86}Sr$ simply originated from water compositional changes within the last 0.1 my? This is very unlikely, because it would demand that the water compositions became homogenized over tens of metres *within* each reservoir interval, generating the very constant $^{87}Sr/^{86}Sr$ values in zones H1-H3 and H5 (Figure 6) yet retaining the distinct step *between* the two reservoirs all within the last 0.1 my. Homogenization of the $^{87}Sr/^{86}Sr$ in the 76 m-thick H1-3 interval by diffusion would take about 44 my (using Equation 2), and over this time period the distinct step change between H5 and H1-3 would have decayed significantly.

780 The main barrier to vertical fluid mixing (Figure 10) must be a barrier to both fluid flow,
781 to explain the pressure data (Figure 2) and diffusive transport to explain the Sr RSA
782 data (Figure 10). Figure 10 provides detail of the lithologies present over the depth
783 interval where the pressure barrier occurs, including representative permeabilities. The
784 non-barrier lithologies in the 3469.5-3478.0 m range (core depth) include sands with
785 ~40 md permeability, and clayey sands, thin shales and coals with much lower
786 permeability (Figure 10). The possible barrier to Sr mixing between samples 10 and 11
787 (Figure 10) occurs across clayey sands, two coals and a thin shale, all of which have
788 low permeabilities and could have contributed to any barrier effect. However, the fact
789 that the two H4 samples (9,10), both situated in clayey sand, have similar $^{87}Sr/^{86}Sr$
790 values suggests that the clayey sands have not acted as barriers. The main $^{87}Sr/^{86}Sr$
791 barrier (between samples 8 and 9) is tightly constrained to a shale (0.1 md) and coal
792 (0.3 md). Shales and coals thus appear to be the main barrier lithologies.

793 Shales and coals can form barriers to pressure, as their high capillary entry pressure
794 and low permeability greatly slows the vertical fluid movement necessary to equilibrate
795 the pressure above and below, and also to diffusive mixing. Shales have low porosity,
796 high tortuosity, and a very high sorption $K_d$ compared to sands, which reduces effective
797 $D$ values (Eq 2). Furthermore, there is evidence (e.g., Shaukat et al., 2005) that Sr
798 sorption onto coal is several orders of magnitude greater than onto shale, which would
799 lead to $D$ values ~3 orders of magnitude less than shale. In a layered package of rocks,
800 the overall $D$ is a thickness-weighted harmonic mean of the individual layer $D$ values
801 (Go et al., 2014), so the low diffusivity of the coal would dominate the barrier effect to Sr
802 diffusion. This indicates that, while the pressure step could be preserved by a

803 combination of shale and coal, it is probably the coal that has the greatest effect on
804 preserving the $^{87}Sr/^{86}Sr$ step.

805 The three lowermost coal layers in H3 (tops at 3408, 3409, 3412 m TVDSS; 3470.5,
806 3471.5, 3473.9 core depth; Figure 6, Figure 9) are not associated with major steps in
807 formation water $^{87}Sr/^{86}Sr$ (Figure 10), in contrast to the spectacular effect of the top-H4
808 layer. There is nothing in the (unpublished) well log data that distinguishes these coals,
809 so it does not seem that it is the physical properties of the top-H4 coal/shale that make it
810 more of a barrier than the underlying coals and shales. The H4 and H3 intervals contain
811 laterally extensive lower coastal plain deposits with interdistributary bays (coals/shales),
812 crevasse splays (fine sandstones/silts) and distributary channel fills (sandstones). The
813 main difference between the top-H4 coal in and the underlying coals is that this bed is
814 immediately overlain by a flooding surface representing a return to shoreface deposition
815 followed by a gradual sea level transgression of the entire system throughout deposition
816 of the H5 interval. So, while there is no evidence for the top-H4 coal/shale layers being
817 more laterally extensive and/or continuous than the underlying H3 coals and shales at
818 the time of deposition, it is possible that the subsequent flooding protected the top-H4
819 coal/shale from subsequent erosion, for example by downcutting distributary channels.
820 The lateral continuity of the top-H4 coal/shale may thus be better preserved. If the
821 secondary barrier (Figure 10) is caused by the top-H3 coal, we note that this is also
822 overlain by a transgressive surface (Figure 2) that could have protected it from
823 subsequent erosion.

824 Similar compositional steps in formation water $^{87}Sr/^{86}Sr$ composition have been
825 revealed by numerous other Sr RSA studies (32 step patterns were documented in

826 Smalley et al., 2020), in many cases with corroborative evidence for a significant barrier
827 effect. The most comparable is from well 13/28A-5 in the Ross Field (UKCS), which
828 displays an almost identical Sr RSA profile to that found in the present study, with very
829 uniform patterns separated by a large step, in this case also across a thin coal and
830 shale interval (Smalley & Hale, 1996). In that example, the Sr RSA data were reinforced
831 by changes on oil composition above and below, indicating that the barrier could have
832 affected the oil filling history. In the Ross field, sedimentological and biostratigraphic
833 analysis indicated the coal was followed by a sharp drop in sediment base level from
834 fluvial to lagoonal, and this, together with evidence that the coal and shale can be
835 correlated across multiple wells several km apart, indicated this to be a laterally very
836 extensive and continuous feature.

837 Mearns & McBride (1999) also report numerous Sr RSA steps in the Dunbar, Thelma
838 and Janice oil fields, UKCS (United Kingdom Continental Shelf). Sr RSA steps in the
839 Dunbar field (Middle Jurassic Brent Group reservoir) occur across thin coal layers within
840 and at the top of the Ness Formation, which is the northward equivalent of the Sleipner
841 formation in the current study area. These coals are associated with small pressure
842 offsets indicative of a significant barrier effect. In the Thelma (Upper Jurassic Brae
843 Formation reservoir) and Janice (Upper Jurassic Fulmar Formation reservoir) fields
844 there are also large $^{87}Sr/^{86}Sr$ steps across thin shales, again associated with small
845 pressure offsets indicating a flow barrier.

846 A large step in water $^{87}Sr/^{86}Sr$ composition was observed in the De Geerdalen aquifer in
847 the Longyearbyen $CO_2$ Laboratory on Svalbard (Huq et al., 2017). The compositional
848 step occurred across lagoonal mudrocks of likely wide lateral extent. In this example,

849 there is a 48 bar pressure discontinuity across the barrier interval, indicating a major
850 barrier to pressure mixing that would probably have a significant impact on the
851 movement of any $CO_2$ injected for storage below this barrier.

852 Overall, then, where large steps in Sr RSA $^{87}Sr/^{86}Sr$ have been observed over short
853 depth ranges this has almost always been across shale and/or coal layers where there
854 is independent evidence for wide lateral extent (from sedimentological or stratigraphic
855 data) and pressure discontinuity indicating barriers to vertical fluid flow. In the cited
856 published studies, as in the current study, there are other shale or coal layers that have
857 either no or very small $^{87}Sr/^{86}Sr$ steps across them, and these are not associated with
858 pressure breaks. This corroborates the interpretation that the main pressure barrier in
859 the studied well is likely to be the coal and/or shale layer across which there is a
860 dramatic $^{87}Sr/^{86}Sr$ step, at the top of H4.

861 **5.4 How long has the barrier effect persisted?**
862

863 The barrier that causes both the pressure break and water $^{87}Sr/^{86}Sr$ step (Figure 6)
864 between the H1-3 and H5 intervals is probably the coal and shale beds at the top of H4
865 (~3494 m TVDSS), perhaps with contributions from the coal layer near the top of H3.
866 The features causing the barrier are thus depositional features that have been present
867 throughout the geological history of the Hugin reservoir. To ascertain how long they did
868 actually act as a barrier to vertical fluid movement, important evidence comes from the
869 carbonate cements.

870 Figure 11 shows the $^{87}Sr/^{86}Sr$ and $\delta^{18}O$ values of the analysed carbonate cements.
871 Samples span the range of depths from above (zone H5) and below (H1-3) the barrier

872 (note, there are no carbonate samples from H4). Remarkably, the $^{87}Sr/^{86}Sr$ of the H5
873 cements plot mainly within the mean ± 2σ range established for present day formation
874 waters in H5 (Figure 6), irrespective of whether they are at the early (low temperature)
875 or late (high temperature) end of the spectrum as defined by the O isotopes. The same
876 goes for the H1-3 samples, where 16 of the 19 samples plot on the H1-3 formation
877 water $^{87}Sr/^{86}Sr$ range of ~0.713 irrespective of cement precipitation time and
878 temperature. There is thus a strong implication that the current step in $^{87}Sr/^{86}Sr$ between
879 H1-3 and H5 has persisted over the cementation history and until the present day. The
880 earliest cements precipitated at ~162 Ma at depths of only a few hundred metres, so the
881 barrier caused by the top-H4 coal/shale, with or without help from the upper H3 coals,
882 has been effective in separating waters of differing composition over much of the burial
883 history of the Hugin Formation, possibly for 162 my.

884 It is likely that the long-lived difference in water $^{87}Sr/^{86}Sr$ between H5 and H1-3 is
885 related to the water composition being buffered by reservoirs of Sr with different
886 $^{87}Sr/^{86}Sr$. However, it is not possible to discriminate whether the carbonates buffer the
887 water, or whether the carbonates simply inherited the water composition that was
888 buffered by dissolution of detrital minerals, such as feldspar or clays.

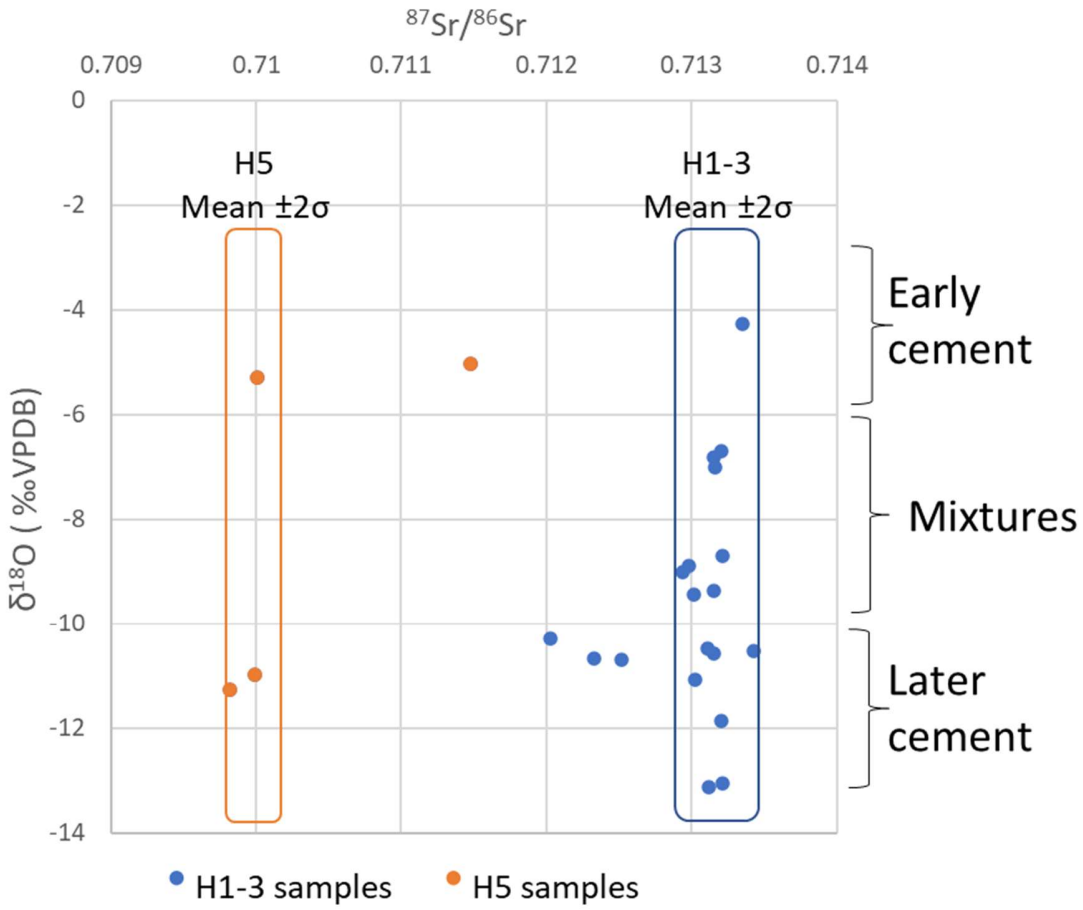


**Figure 11. Sr and O isotopes in carbonate samples. The $^{87}Sr/^{86}Sr$ ranges for the H5 and H1-3 intervals (from Figure 6) are represented in samples at both the early and late ends of the age spectrum, indicating that the difference in Sr isotopes has persisted for much of the cementation history.**

## 6. Conclusions

Pressure data from well 25/2-18 ST2 in the Langfjellet Oil Discovery indicate a barrier in the Hugin formation reservoir somewhere within a 25 m depth interval, suggesting the presence of a barrier to vertical fluid flow. There are several potential candidates for the inferred barrier, consisting of shale and coal layers. A study of current formation water composition profiles using $^{87}Sr/^{86}Sr$ as a tracer sampled by Sr RSA, combined with Sr,

C and O isotope analysis of carbonate cements, was used to investigate the position and nature of the barrier, and whether other features (heavily carbonate-cemented zones) may also have barrier effects. The data revealed three populations of water in the Hugin Formation reservoir, in zones H1-3, H4, and H5. Within the depth interval where the pressure barrier is located, there is a small but statistically significant step in water $^{87}Sr/^{86}Sr$ composition across a package of shales and coals near the top of H3, and a very large step across a ~1 m-thick shale/coal layer at the H4-H5 boundary. Both of these features could contribute to the barrier effect, but the size of the compositional step at the top of H4 points to this shale/coal layer as being the main influence. The H4-H5 boundary is interpreted as a flooding surface, which reflects a rise in relative water level that could have helped preserve the lateral continuity of the barrier shale/coal immediately underneath by protecting it from subsequent erosion. Modelling of diffusive mixing of the water compositional step indicates that the pressure barrier is also a barrier to Sr diffusion.

Carbonate cements were examined to determine whether the current water compositional patterns extended back through time. The carbonates formed in at least two episodes:

- Early, at ~30ºC, in the zone of bacterial methanogenesis. This cement is pre-compactional and formed at no more than a few hundred metres burial depth, at ~162 Ma, only 5 my or so after deposition.
- Late, at ~90ºC with a contribution of carbon derived from thermal decarboxylation. This cement precipitated at ~46 Ma when the rocks were buried to a depth of ~2500m.

The $^{87}Sr/^{86}Sr$ data for the carbonate cements reveal the same populations as the Sr RSA data in zones H1-3 and H5. The compositional stratification of the formation water must thus have been present when the early cements were precipitated (~162 Ma), when the late cements were precipitated (~46 Ma) down till today. The persistence of this compositional step for most of the geological history of the rocks confirms the presence of a major fluid communication barrier.

Several heavily carbonate-cemented intervals are present. The Sr RSA data shows no deviation in water composition whatsoever across these intervals. This implies that the cemented intervals are unlikely to form extensive barriers, although their behaviour as local flow baffles cannot be ruled out.

The combination of pressure data (to identify pressure barriers), with formation water $^{87}Sr/^{86}Sr$ sampled by Sr RSA (to add spatial resolution and to pinpoint barriers to Sr diffusion) and Sr-C-O isotopes of carbonates (to determine formation water $^{87}Sr/^{86}Sr$ back through time) is a powerful approach for identifying major long-term fluid communication barriers and for differentiating them from smaller, less effective or shorter-lived features. This has applications in identifying seals that might act as caprocks in oil migration and trapping for oil exploration, flow barriers or baffles in oil and gas production or water resources management, and also in underground storage of $CO_2$ or radioactive waste, where understanding the long-term effectiveness of caprocks to maintain isolation of the undesired material is critical.

## Acknowledgments

We thank Aker BP for permission to publish the results along with background information on the Langfjellet Discovery. The authors would like to thank Stephane Polteau for his useful comments.

## References

Antonellini, M.A., Aydin, A. & Orr, L. 1999. Outcrop aided characterization of a faulted hydrocarbon reservoir: Arroyo Grande oil field, California, USA. In: Haneberg, W.C., Mozley, P.S., Moore, C.J. & Goodwin, L.B. (eds) Faults and Subsurface Fluid Flow. American Geophysical Union, Washington, Geophysical Monograph, 113, 7– 26.

Barrie, G.M, Worden, R.H., Barrie, C.D. and Boyce, A.J. (2015). Extensive evaporation in a modern temperate estuary: stable isotope and compositional evidence. Limnology and Oceanography, 60, 1241-1250.

Basin, P., Brigaud, B., Durlet, C., Deconinck, J., Vincent, B., Thierry, J., Trouiller, A., (2009). The origin and timing of multiphase cementation in carbonates : impact of regional scale geodynamic events on the Middle Jurassic Limestones diagenesis. Sediment. Geol. 222, 161–180.

Bjørlykke, K. (2010). Petroleum Geoscienece: From Sedimentary Environments to Rock Physics. Springer, Heidelberg, Dordrecht, London, New York, 507pp.

Brommundt, J., T. U. Kaempfer, C. P. Enssle, G. Mayer, and J. Wendling (2014), Full-scale 3D modelling of a nuclear waste repository in the Callovo-Oxfordian clay. Part 1: thermo-hydraulic two-phase transport of water and hydrogen, Geol Soc Spec Publ, 400, 443-467, doi:10.1144/Sp400.34.

Carslaw, H. S., and J. C. Jaeger (1959). Conduction of heat in solids: Oxford, England, Oxford Science Publications, 510 p.

Cavanagh, A. J., and Haszeldine, R. S. (2014). The Sleipner storage site: Capillary flow modeling of a layered $CO_2$ plume requires fractured shale barriers within the Utsira Formation. International Journal of Greenhouse Gas Control, 21, 101-112.

Choi, J.-H., Edwards, P., Ko, K. and Kim, Y.-S. (2015). Definition and classification of fault damage zones: A review and a new methodological approach. Earth-Science Reviews, 152, 70-87.

Coplen, T.B., Kendall, C. and Hopple, J. (1983). Comparison of stable isotope reference samples. Nature, 302, pp. 236-238.

980 Cui, Y., Jones, S. J., Saville, C., Stricker, S., Wang, G., Tang, L., Fan, X. and Chen, J.
981 (2017). The role played by carbonate cementation in controlling reservoir quality of
982 the Triassic Skagerrak Formation, Norway. Marine and Petroleum Geology, 85,
983 316-331.

984 Dale, A., John, C.M., Mozley, P.S., Smalley, P.C. & Muggeridge, A.H. (2014). Time-
985 capsule concretions :Unlocking burial diagenetic processes in the Mancos Shale
986 using carbonate clumped isotopes. Earth and Planetary Science Letters 394, 30-
987 37.

988 Doughty, C., Freifeld, B. M., and Trautz, R. C. (2008). Site characterization for $CO_2$
989 geologic storage and vice versa: the Frio brine pilot, Texas, USA as a case study.
990 Environmental Geology, 54, 1635–1656.

991 Dutton, S. P., White, C. D., Willis, B. J., and Novakovic, D. (2002). Calcite cement
992 distribution and its effect on fluid flow in a deltaic sandstone, Frontier Formation,
993 Wyoming. American Association of Petroleum Geologists Bulletin, 86 (12), 2007-
994 2021.

995 Elenius, M., Skurtveit, E., Yarushina, V., Baige, I., Sundale, A., Wangen, M.,
996 Landschulz, K., Kaufmann, R., Choi, J.C., Hellevang, H., Podladchikov, Y.,
997 Aavatsmark, I. and Gasdab, S.E. (2018). Assessment of $CO_2$ storage capacity
998 based on sparse data: Skade Formation. International Journal of Greenhouse Gas
999 Control, 79, 252-271.

1000 Evans, T.R. & Coleman, N.C. (1974). North Sea geothermal gradients. Nature 247, 28-
1001 30.

1002 Fayek, M., Harrison, M., Grove, M., Mckeegan, K. D., Coath, C. D., and Boles, J. R.
1003 (2001). In situ stable isotopic evidence for protracted and complex carbonate
1004 cementation in a petroleum reservoir, North Coles Levee, San Joaquin Basin,
1005 California, U.S.A. Journal of Sedimentary Research, 71 (3), 444-458.

1006 Folkestad, A. and Satur, N. (2008). Regressive and transgressive cycles in a rift-basin:
1007 Depositional model and sedimentary partitioning of the Middle Jurassic Hugin
1008 Formation, Southern Viking Graben, North Sea. Sedimentary Geology 207, 1–21.

1009 Fokker, P. A., Visser, K., Peters, E., Kunakbayeva, G., and Muntendam-Bos, A.G.
1010 (2012). Inversion of surface subsidence data to quantify reservoir
1011 compartmentalization: A field study. Journal of Petroleum Science and
1012 Engineering, 96–97,10–21.

1013 Fox, R.J. and Bowman, M.B.J. (2010). The challenges and impact of
1014 compartmentalization in reservoir appraisal and development. In: Jolley, S.,
1015 Fisher, Q.J., Ainsworth, B., Vrolijk, P. and Delisle, S. (Eds.), Reservoir
1016 Compartmentalization. Geological Society Special Publication 347, 9-23.

Fricke, H.C. and O'Neil, J.R. (1999). The correlation between $^{18}O/^{16}O$ ratios of meteoric water and surface temperature: its use in investigating terrestrial climate change over geologic time. Earth and Planetary Science Letters, 170, 181-196.

Gluyas, J.G. and Cade, C.A. (1997). Prediction of Porosity in Compacted Sands, In: Reservoir Quality Prediction in Sandstones and Carbonates, J. A. Kupecz, J. Gluyas, S. Bloch (eds). AAPG Memoir 69, 19-28.

Go, J., Bortone, I., Muggeridge, A.H. and Smalley, P.C. (2014). Predicting Vertical Flow Barriers Using Tracer Diffusion in Partially Saturated, Layered Porous Media. Transport in Porous Media, 105, 255-276.

Greenwood, P. J., Shaw, H. F., and Fallick, A. E. (1994). Petrographic and isotopic evidence for diagenetic processes in Middle Jurassic sandstones and mudrocks from the Brae Area, North Sea. Clay Minerals, 29 (4), 637-650.

Griffiths, J., Faulkner, D.R., Edwards, A.P. & Worden, R.H. (2016). Deformation band development as a function of intrinsic host-rock properties in Triassic Sherwood Sandstone. In: Armitage, P. J., Butcher, A. R., Churchill, J. M., Csoma, A. E., Hollis, C., Lander, R. H., Omma, J. E. and Worden, R. H. (eds) Reservoir Quality of Clastic and Carbonate Rocks: Analysis, Modelling and Prediction. Geological Society Special Publication 435.

Hartz, E. H., Medvedev, S., and Schmid, D. W. (2017). Development of sedimentary basins: differential stretching, phase transitions, shear heating and tectonic pressure: Basin Research, v. 29, no. 5, p. 591-604.

Hantschel, T., and Kauerauf, A. I. (2009). Fundamentals of basin and petroleum systems modeling, Springer Science & Business Media.

Huq, F., Smalley, P. C., Mørkved, P. T., Johansen, I., Yarushina, V., and Johansen, H. (2017). The Longyearbyen $CO_2$ Lab: fluid communication in reservoir and cap-rock. International Journal of Greenhouse Gas Control, 63 (59-76).

Irwin, H. R., Coleman, M & Curtis, C. (1977). Isotopic evidence for source of diagenetic carbonates formed during burial of organic-rich sediments. Nature 269, 209-213.

Jackson, A., Stright, L., Hubbard, S.M. and Romans, B.W. (2019). Static connectivity of stacked deep-water channel elements constrained by high-resolution digital outcrop models. AAPG Bulletin, 103, 2943-2973.

Japsen, P., Dysthe, D. K., Hartz, E. H., Stipp, S. L. S., Yarushina, V. M. and Jamtveit, B. (2011). A compaction front in North Sea chalk. Journal Geophysical Research-Solid Earth, 116, B11208, doi:10.1029/2011JB008564

Jolley, S. J., Fisher, Q. J., and Ainsworth, R. B. (2010). Reservoir compartmentalization: an introduction. Geological Society, London, Special Publications, 347, 1–8.

Kim, S.-T., and O'Neil, J. R. (1997). Equilibrium and nonequilibrium oxygen isotope effects in synthetic carbonates. Geochimica et Cosmochimica Acta, 61: 3461-3475.

Kieft, R. L., Jackson, C. A. L., Hampson, G. J., and Larsen, E. (2010). Sedimentology and sequence stratigraphy of the Hugin formation, Quadrant 15, Norwegian sector, South Viking Graben. Petroleum Geology Conference series, 7, 157-176.

Klein, J.S., Mozley, P., Campbell, A. & Cole, R. (1999). Spatial distribution of carbon and oxygen isotopes in laterally extensive carbonate-cemented layers: Implications for mode of growth and subsurface identification. Journal of Sedimentary Research, 69, 184-191.

Korte, C., Hesselbo, S. P., Ullmann, C. V., Dietl, G., Ruhl, M., Schweigert, G., and Thibault, N. (2015). Jurassic climate mode governed by ocean gateway: Nature communications, v. 6, p. 10015.

Labus, K., Cicha-Szot, R. and Falkowicz, S. (2020). Injected silicate horizontal barriers for protection of shallow groundwater - Technological and geochemical issues. Applied Geochemistry, 116, 104577.

Liang, H., Xu,F., Xu, G., Yuan, H., Huang, S., Wang, Y., Wang, L., Fu, D. (2019). Geochemical characteristics and origins of the diagenetic fluids of the Permian Changxing Formation calcites in the Southeastern Sichuan Basin: Evidence from petrography, inclusions and Sr, C and O isotopes. Marine and Petroleum Geology 103, 564–580.

Li, K., Cai, C., He, H., Jiang, L., Cai, L., Xiang, L., Huang, S., and Zhang, C. (2011). Origin of palaeo-waters in the Ordovician carbonates in Tahe oilfield, Tarim Basin: constraints from fluid inclusions and Sr, C and O isotopes. Geofluids 11, 71–86.

Løseth, H., Gading, M. and Wensaas, L. (2009). Hydrocarbon leakage interpreted on seismic data, Marine and Petroleum Geology, 26, 1304-1319.

McArthur, J.M., Howarth, R.H. & Bailey, T.R (2001). Strontium Isotope Stratigraphy: LOWESS Version 3: Best Fit to the Marine Sr-Isotope Curve for 0–509 Ma and Accompanying Look-up Table for Deriving Numerical Age. Journal of Geology 109, 155-170.

McCartney, R.A. and Rein, E. (2005). Formation waters of the Norwegian Continental Shelf. Proceedings of the 16th International Symposium on Oilfield Chemistry, Geilo, Norway, 13-16 March 2005. http://oilfieldwaterservices.co.uk/wp-content/uploads/2014/05/McCartney-and-Rein-2005.pdf

Mearns E.W. and McBride J.J. (1999). Hydrocarbon filling history and reservoir continuity of oil fields evaluated using $^{87}Sr/^{86}Sr$ isotope ratio variations in formation water, with examples from the North Sea. Petroleum Geoscience, 5, p. 17-27.

Ramm, M. (1992). Porosity-depth trends in reservoir sandstones: theoretical models related to Jurassic sandstones offshore Norway. Marine and Petroleum Geology 9, 553-567.

Royer, D. L., Berner, R. A., Montañez, I. P., Tabor, N. J., and Beerling, D. J. (2004). Co~ 2 as a primary driver of phanerozoic climate: GSA today, v. 14, no. 3, p. 4-10.

Rüpke, L. H., Schmid, D. W., Perez-Gussinye, M., and Hartz, E. (2013). Interrelation between rifting, faulting, sedimentation, and mantle serpentinization during continental margin formation—including examples from the Norwegian Sea: Geochemistry, Geophysics, Geosystems, v. 14, no. 10, p. 4351-4369.

Sampei, Y., Matsumoto, E., Dettman, D.L., Tokuoka, T. and Abe, O. (2005). Paleosalinity in a brackish lake during the Holocene based on stable oxygen and carbon isotopes of shell carbonate in Nakaumi Lagoon, southwest Japan. Palaeogeography, Palaeoclimatology, Palaeoecology, 224, 352-366.

Schoell, M., Jenden, P.O., Beeunas, M.A., and Coleman, D.O. (1993). Isotope Analyses of Gases in Gas Field and Gas Storage Operations. Society of Petroleum Engineers, SPE Gas Technology Symposium, 28-30 June, Calgary, Alberta, Canada.

Shackleton, N.J. and Kennett, J.P. (1975). Paleotemperature history of the Cenozoic and the initiation of Antarctic glaciation: oxygen and carbon isotope analyses in DSDP sites 277, 279, and 281. Initial Rep. Deep Sea Drill. Proj., 29 (1975), pp. 743-755.

Shaukat, M. S., Sarwar, M. I. and Qadeer, R. (2005). Adsorption of strontium ions from aqueous solution on Pakistani coal. Journal of Radioanalytical and Nuclear Chemistry, 265, 73-79.

Skaare, B.B., Kihle, J. & Torsvik, T. (2011). Biodegradation of Crude Oil as Potential Source of Organic Acids in Produced Water. In Produced Water, pp 115-126, Lee, K. & Neff, J. (eds.) Springer Science + Business Media, LLC.

Skurtveit, E., Torabi, A., Alikarami, R., & Braathen, A. (2015). Fault baffle to conduit developments: Reactivation and calcite cementation of deformation band fault in aeolian sandstone. Petroleum Geoscience, 21, 3-16.

Smalley, P.C., Dodd, T.A., Stockden, I. L., Råheim, A., and Mearns, E. W. (1995). Compositional heterogeneities in oilfield formation waters: identifying them, using them. Geological Society, London, Special Publications, 86:59-69.

Smalley, P.C. & Hale, N.A. (1996). Early identification of reservoir compartmentalization by combining a range of conventional and novel data types. Society of Petroleum Engineers, Formation Evaluation. September 1996, 163-169.

Smalley, P.C. & Muggeridge, A.H. (2010). Reservoir compartmentalization – Get it before it gets you. In: Jolley, S., Fisher, Q.J., Ainsworth, B., Vrolijk, P. and Delisle, S. (Eds.), Reservoir Compartmentalization. Geological Society Special Publication 347, 43-53.

Smalley, P.C., Muggeridge, A.H. & Kusuma, C.R. (2020). Patterns of water $^{87}Sr/^{86}Sr$ variations in oil-, gas- and water-saturated rocks: implications for fluid communication processes, distances and timescales. Marine and Petroleum Geology, 122, paper 104678. https://doi.org/10.1016/j.marpetgeo.2020.104678.

Souche, A., Schmid, D. W., and Rüpke, L., 2017, Interrelation between surface and basement heat flow in sedimentary basins: AAPG Bulletin, v. 101, no. 10, p. 1697-1713.

Torabi, A., Braathen, A., Cuisiat, F. and Fossen, H. (2007). S

hear zones in porous sand: Insights from ring-shear experiments and naturally deformed sandstones. Tectonophysics, 437, 37-50.

Toussaint, R., Aharonov, E., Koehn, D., Gratier, P., Ebner, M., Baud, P., Rolland, A. and Renard, F. (2018). Stylolites: A review. Journal of Structural Geology, 114, 163-195.

Walderhaug, O. and Bjørkum, P. A. (1992). Effect of meteoric water flow on calcite cementation in the Middle Jurassic Oseberg Formation, well 30/3-2, Veslefrikk Field, Norwegian North Sea.

Wangen, M. (2010). Physical principles of sedimentary basin analysis. Cambridge University Press, Cambridge, UK ; New York, 527 pp.

Warren, E.A. and Smalley, P.C. (1994). North Sea Formation Waters Atlas. Geological Society of London Memoir 15, 208pp.

Whiticar, M.J. (1999). Carbon and hydrogen isotope systematics of bacterial formation and oxidation of methane. Chemical Geology, 161, 291-314.

Woods, A.W. (2015). Flow in Porous Rocks: Energy and Environmental Applications. Cambridge University Press, 289pp.

Worden, R.H., Morrall, G.T., Kelly, S., McArdle. P. and Barshep, D.V. (2019). A renewed look at calcite cement in marine-deltaic sandstones: the Brent Reservoir, Heather Field, northern North Sea, UK. Geological Society, London, Special Publications, 484, https://doi.org/10.1144/SP484-2018-43